RESONANCE ZONES ON THE SURFACE OF A DIPPING LAYER DUE TO PLANE SH SEISMIC INPUT

By

G. L. Wojcik

WEIDLINGER ASSOCIATES, CONSULTING ENGINEERS
3000 Sand Hill Road
Suite 245, Building 4
Menlo Park, California 94025

-and-

110 East 59th Street
New York, New York 10022

Grant Report No. 11

Prepared for

National Science Foundation (ASRA Directorate)
1800 G Street
Washington, D. C. 20550

Grant No. PFR 78-15049

January 1979

50272-101

REPORT DOCUMENTATION PAGE

1. REPORT NO. NSF/RA-790200

2.

3. Recipient's Accession No. PB 80 107907

4. Title and Subtitle
Resonance Zones on the Surface of a Dipping Layer Due to Plane SH Seismic Input

5. Report Date January 1979

6.

7. Author(s) G. L. Wojcik

8. Performing Organization Rept. No. 11

9. Performing Organization Name and Address

Weidlinger Associates, Consulting Engineers
110 East 58th Street
New York, New York 10022

10. Project/Task/Work Unit No.

11. Contract(C) or Grant(G) No.
(C)
(G) PFR7815049

12. Sponsoring Organization Name and Address

Engineering and Applied Science (EAS)
National Science Foundation
1800 G Street, N.W.
Washington, D.C. 20550

13. Type of Report & Period Covered

14.

15. Supplementary Notes

16. Abstract (Limit: 200 words)

This is an analytical study of the local effects of lateral geologic inhomogeneity on surface ground motion during earthquakes. The model is a surface dipping layer overlaying a halfspace, with plane SH waves incident from the halfspace in the downdip direction. Surface motion over the layer is calculated for transient (time domain) and harmonic (frequency domain) inputs. In the frequency domain constructive interference on the surface produces a standing wave pattern with spatial zones of resonance where translational motion is on the order of 6-15 times that if the dipping layer were not present. Rotational motion is amplified to a greater extent, on the order of 20-50 times, and relative motion between spatially separated points, on the order of 10-20 times. The amplification mechanism is total reflection of multiple reflected plane waves between the free surface and halfspace. In the time domain a transient input is converted to a series of transients on the surface. Depending on the natural frequency and location of the layer, structural or instrument response to a transient input is amplified to the same degree that surface motion is amplified in the frequency domain. An extension of the analysis, suitable for Love wave excitation, is described. Applications include seismic zonation, critical facility siting, building rehabilitation and ground failure.

17. Document Analysis a. Descriptors

Earthquakes
Dynamic response
Dynamic structural analysis
Seismic waves
Plane waves
Shock waves
Love waves

b. Identifiers/Open-Ended Terms

Lateral geologic inhomogeneity
Surface ground motion
Time domain
Frequency domain
Dipping layer

c. COSATI Field/Group

18. Availability Statement NTIS

19. Security Class (This Report)

20. Security Class (This Page)

21. No. of Pages 99

22. Price A05-A01

(See ANSI-Z39.18) *See Instructions on Reverse* **OPTIONAL FORM 272** (4-77)
(Formerly NTIS-35)
Department of Commerce

ACKNOWLEDGMENT

I am grateful for the comments and support of a number of individuals during the course of the work reported here, particularly my colleagues, Jeremy Isenberg, Joseph P. Wright and Melvin L. Baron. David M. Boore at Stanford deserves special thanks for pointing out the Skopje, 1963 earthquake and other references, and his comments on relevant free-field calculations. Also, the respective efforts of Myrtle Carey and Penny Sevison in typing and illustrating the report are gratefully acknowledged.

ABSTRACT

This is an analytical study of the local effects of lateral geologic inhomogeneity on surface ground motion during earthquakes. The model is a surface dipping layer overlaying a halfspace, with plane SH waves incident from the halfspace in the downdip direction. Surface motion over the layer is calculated for transient (time domain) and harmonic (frequency domain) inputs. In the frequency domain constructive interference on the surface produces a standing wave pattern with spatial zones of resonance where translational motion is on the order of 6-15 times that if the dipping layer were not present. Rotational motion is amplified to a greater extent, on the order of 20-50 times, and relative motion between spatially separated points, on the order of 10-20 times. The amplification mechanism is total reflection of multiply reflected plane waves between the free surface and halfspace. In the time domain a transient input is converted to a series of transients on the surface. Depending on the natural frequency and location of the layer, structural or instrument response to a transient input is amplified to the same degree that surface motion is amplified in the frequency domain. An extension of the analyisis, suitable for Love wave excitation, is described. Applications include seismic zonation, critical facility siting, building rehabilitation and ground failure.

CONTENTS

INTRODUCTION 1

- Scope 1
- Approach 1
- Results 2
- Motivation 2

REFERENCES - INTRODUCTION 4

PART I — A SURVEY OF THE SEISMOLOGICAL LITERATURE ON EFFECTS OF NEAR-SURFACE LATERAL INHOMOGENEITY 5

- Analytical Studies 5
- Numerical Modeling Studies 11
- Experimental Modeling Studies 13
- Field Studies 14
- Discussion 15
- Conclusions 20

REFERENCES - PART I 22

PART II — SURFACE DIPPING LAYER RESPONSE DUE TO INCIDENT PLANE SH WAVES 24

TIME DOMAIN WEDGE RESPONSE 26

- Self-Similar Solutions 27
- Plane Wave Solutions in the Hyperbolic Domain 29
- Diffracted Solutions in the Elliptic Domain 32
- Time Domain Response Spectra 33

FREQUENCY DOMAIN WEDGE RESPONSE 34

- The Amplitude Spectrum: Translational Surface Motion 39
- The Phase Spectrum: Rotational and Relative Surface Motion 42

APPROXIMATE SOLUTIONS FOR THE DIPPING LAYER 50

- Time Domain Analysis of the Primary Wave System 52
- Frequency Domain Analysis of the Primary Wave System 53

REFERENCES - PART II 61

CONCLUSION 62

- Summary 62
- Discussion 65
- Conclusions 69

REFERENCES - CONCLUSION 72

CONTENTS (CONTINUED)

APPENDIX A — REFLECTION AND REFRACTION OF PLANE SH WAVES 73

Case 1: Subcritical reflection of a plane step 75
Case 2: Supercritical reflection of a plane step 77
Case 3: Supercritical reflection of a supercritically-reflected plane step 78

APPENDIX B — SELF-SIMILAR WEDGE SOLUTIONS IN THE HYPERBOLIC DOMAIN 80

APPENDIX C — SELF-SIMILAR WEDGE SOLUTIONS IN THE ELLIPTIC DOMAIN 85

ILLUSTRATIONS

Figure		Page
1	a) Horizontally layered halfspace model. b) Laterally inhomogeneous halfspace model.	6
2	a) Shallow alluvial basin, A & L (1970). b) Step in the Moho discontinuity, A & L (1970). c) Dipping transition layer, H & H (1977).	8
3	Comparison between downdip and updip propagation.	10
4	Cross sections through the most heavily damaged sections in Skopje (from Poceski (1969)).	16
5	a) Dipping transition layer. b) Alluvial basin. c) Surface dipping layer.	18
6	The surface dipping layer problem.	25
7	The incident and transmitted wave system.	25
8	The wedge coordinate system.	28
9	Characteristics in the hyperbolic domain.	30
10	Semi-infinite strip in the complex α plane.	30
11	Plane wave solutions in the hyperbolic domain and surface response including the diffracted wave.	31
12	The normalized velocity amplitude spectrum for various wedge angles, with $V_o = 3c$.	37
13	The normalized velocity phase spectrum for various wedge angles, with $V_o = 3c$.	38
14	Peak normalized velocity for a range of wedge angles, γ, and interface phase velocities, V_o.	
15	A representative velocity amplitude spectrum with and without the diffracted wave ($\gamma = 3^\circ$, $V_o = 3c$).	41
16	A representative amplitude spectrum in the higher frequency range ($\gamma = 3^\circ$, $V_o = 3c$).	43
17	The normalized rotation amplitude spectrum for various wedge angles, with $V_o = 3c$ (note, $\psi = A_R/V_o$).	44

ILLUSTRATIONS (CONTINUED)

Figure Page

18 Peak normalized rotation for a range of wedge angles, γ, and interface phase velocities, V_o. 46

19 A representative rotation amplitude spectrum with and without the diffracted wave ($\gamma = 3^\circ$, $V_o = 3c$).

20 A representative velocity phase spectrum derivative with and without the diffracted wave ($\gamma = 3^\circ$, $V_o = 3c$). 48

21 The relative velocity spectrum for various gagelengths ($\gamma = 3^\circ$, $V_o = 3c$). 49

22 The complete wave system in the dipping layer and halfspace ($\gamma = 28^\circ$, $\bar{c}/c = 2$, $\bar{\delta} = 40^\circ$). 51

23 Approximate velocity amplitude spectra for moderate dip angles, with $\bar{c}/c = 3$, $\bar{\rho}/\rho = 1.27$. 55

24 Variation of peak normalized velocity, with incidence angle, for $\gamma = 3^\circ$, $\bar{c}/c = 3.75$, $\bar{\rho}/\rho = 1.27$. 57

25 Variation of peak normalized velocity with incidence angle, for $\gamma = 1^\circ$, $\bar{c}/c = 3$, $\bar{\rho}/\rho = 1.27$. The dashed curve shows the trend of 1-D theory. 58

26 Variation of peak normalized velocity with wavespeed ratio, $\bar{c}/c$, for a range of dip angles, γ, with $\bar{\rho}/\rho = 1.27$. 60

27 A schematic of Love wave propagation in a surface layer overlain by a dipping layer. 68

A-1 Plane SH wave incident on a material interface ($y = 0$). 74

A-2 Characteristics for the case of subcritical reflection. 76

A-3 Characteristics for the case of supercritical reflection. 76

B-1 Wave system (characteristics) for a wedge angle, $\gamma = 28^\circ$ and $V_o/c = 3$. 81

B-2 Plane waves and velocity response for $\gamma = 28^\circ$ and $\gamma = 20^\circ$ ($V_o/c = 3$). 84

C-1 Succession of mappings from the physical domain to the α and ζ complex planes. 86

INTRODUCTION

Scope

This is a study of the local effects of lateral geologic inhomogeneity on surface ground motion during earthquakes. Part I comprises a brief review of the seismological literature and examines relevant analytical, numerical, experimental and field studies. Motivated by results of the survey, Part II presents an analysis of the most basic, yet realistic, two-dimensional laterally inhomogeneous halfspace model—the surface dipping layer with plane SH waves incident from below. This geometry is an idealization of the dipping transition layer, a common geologic formation. Of interest is the modification of surface motion over the layer in both the time and frequency domain, i.e. for transient and harmonic inputs. Translational, rotational and relative surface motions are calculated.

Approach

Considerable analytical advantage is gained by idealizing the class of dipping transition layers as a surface dipping layer, i.e. as a shallow wedge of softer material overlaying a harder obtuse wedge or halfspace. The dipping layer does not have a characteristic length and mathematically this reduces the number of independent variables by virtue of dynamic- or self-similarity. The result is a system of elastodynamic equations which can be solved using the method of characteristics and analytic function theory, rather than classical transform methods which are comparatively cumbersome. The soft wedge, decoupled from the halfspace, is analyzed first to determine the nature of the diffracted and plane wave system, followed by an approximate analysis of the coupled problem. Surface response is calculated for a transient input, from which frequency domain response is found by convolution.

Results

The principal feature of surface effects due to the dipping layer is marked enhancement of ground motion in either the time or frequency domain. In the frequency domain, constructive interference on the surface produces a standing wave pattern with zones of resonance where translational motion is on the order of 6-15 times that found if the layer were not present. Rotational motion is amplified on the order of 20-50 times the free-field response, and relative motion on the order of 10-20 times. The highest amplifications occur for small dip angles, e.g. $\leq 4^{\circ}$. The mechanism for this behavior is total reflection of multiply reflected plane waves between the free surface and interface. In the time domain a transient input is converted to a series of transients, one for each free surface reflection of the trapped wave. Structural or instrument response to a transient input is amplified to the same degree that surface motion is amplified for harmonic input. An extension of this analysis, suitable for Love wave inputs is described in the Conclusion. A complete summary, along with a discussion of applications and conclusions are also presented there. Potential applications of the dipping layer solution and its extensions include ranking of sites on the basis of subsurface geology with the view to seismic safety. For sites with dipping interfaces, comparative response over the site can be assessed by assuming a range of body or surface wave inputs. In this sense absolute estimates of seismic input may prove to be unnecessary.

Motivation

This study was prompted by an ongoing interest in effects of a dipping layer, e.g. Wojcik (1977), and an application to the seismic response of buried water pipelines. The application was based on an observation in the 1971 San

Fernando earthquake that water pipes near the southern edge of San Fernando Valley received greater damage than similar pipelines in the central valley, nearer the epicenter. Under the present NSF grant, several explanations were considered by Isenberg (1978) and basic data on differences in physical condition of the pipelines collected. It was suspected that local geologic features, such as nonuniform layering or proximity to the edge of the valley, might have produced anomalous relative ground motion to which extended, segmented pipelines are vulnerable. This suspicion was encouraged by observations in the 1963 Skopje earthquake that lateral inhomogeneities and structural damage were strongly correlated, Poceski (1969). A likely mechanism was found in work by Hong and Helmberger (1977) where significant effects, from a seismological rather than strong motion viewpoint, were shown for a dipping transition layer over a halfspace with waves incident in the downdip, i.e. diverging, direction. These observations suggested the more complete literature survey included here, Part I.

REFERENCES - INTRODUCTION

Hong, T. L. and D. V. Helmberger (1977). Generalized ray theory for dipping structure, Bull. Seism. Soc. Am. 67, 995-1008.

Isenberg, J. (1978). Seismic performance of underground water pipelines in the southeast San Fernando Valley in the 1971 San Fernando earthquake, Weidlinger Associates, Grant Report 8, NSF (ASRA Directorate). Grant PFR 78-15049.

Poceski, A. (1969). The ground effects of the Skopje July 26, 1963 earthquake, Bull. Seism. Soc. Am. 59, 1-22.

Wojcik, G. L. (1977). Self-similar elastodynamic solutions for the plane wedge, Ph.D. thesis, Caltech.

PART I

A SURVEY OF THE SEISMOLOGICAL LITERATURE ON EFFECTS OF NEAR-SURFACE LATERAL INHOMOGENEITY

In earthquake engineering and strong motion seismology, many models of the upper crust use a horizontally layered, linear elastic (or viscoelastic) halfspace approximation, Fig. 1a, to investigate free field surface response. Various analytical schemes based on separability and the superposition principle can then be used to determine response for arbitrary input. Although these layered models are useful and valid in many situations, laterally inhomogeneous models often are more realistic, Fig. 1b. Unfortunately, the latter are not amenable to any exact analytical approach, except for certain degenerate geometries with scalar motion (i.e. a single component of displacement as for SH waves). In the following, results of a brief literature survey on seismic problems involving laterally inhomogeneous halfspace models are described. Only those papers dealing with geometries or techniques with some bearing on earthquake response in the neighborhood of near-surface lateral inhomogeneities are examined (e.g. classical scattering or diffraction type problems are excluded). Analytical, numerical, experimental and field studies are described in that order, followed by a discussion and conclusions motivating Part II.

Analytical Studies

Exact solutions for a halfspace with lateral inhomogeneities near the surface are extremely difficult. This is due to characteristic lengths and associated resonances introduced by the inhomogeneity, as well as the coupling between P and S waves at material interfaces and boundaries. For the case when only one wave type exists, e.g. SH waves or P waves under an acoustic approximation, certain realistic geometries can be solved. Generally, physical and rational mathematical approximations must be employed.

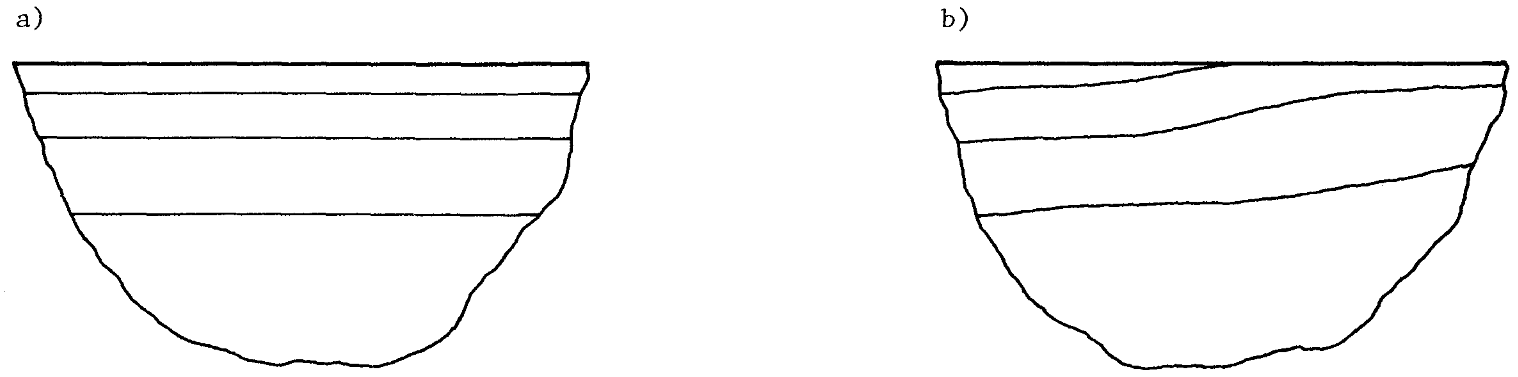

Figure 1. a) Horizontally layered halfspace model.
b) Laterally inhomogeneous halfspace model.

Notable in the context of exact solutions are papers by Trifunac (1971) and Wong and Trifunac (1974) on surface motion of 2-D semi-cylindrical and semi-elliptical alluvial basins, respectively, for incident plane harmonic SH waves. The authors found that, through constructive and destructive interference in the basin, surface displacement amplitude changed rapidly over short distances, varying as much as an order of magnitude, and that both the distribution and amplitude were strongly dependent on frequency and angle of incidence.

Although informative, the above approach is only applicable to a restricted class of surface inclusions. A more general approach, no longer exact but relying on a rational approximation (formulated in principle by Rayleigh), is contained in a paper by Aki and Larner (1970). They investigated the 2-D surface motion of a layer over a halfspace with irregular interface, subject to SH inputs from the halfspace at arbitrary angle. The scattered wavefield was represented by a linear combination of plane waves with discrete horizontal wavenumbers and the coefficients determined by satisfaction of boundary conditions (in a least-squares sense) in the wavenumber domain (utilizing the FFT). There were two major motivations, namely the study of crustal structure and the ground motion problem. For the latter, surface displacements were obtained for soft basins with relatively long wavelength SH waves incident at arbitrary angle. It was found that more energy was trapped by the basin for shallow incidence angles, in contrast to vertical incidence, Fig. 2a, and that lateral amplitude variations (by a factor of 2) were quite pronounced over the surface of flat, soft basins. From the viewpoint of crustal structure studies, models of the Moho discontinuity with dimpled and stepped irregularities, e.g. Fig. 2b, were examined. Whereas in the basin the surface displacements were due primarily to resonance effects, surface displace-

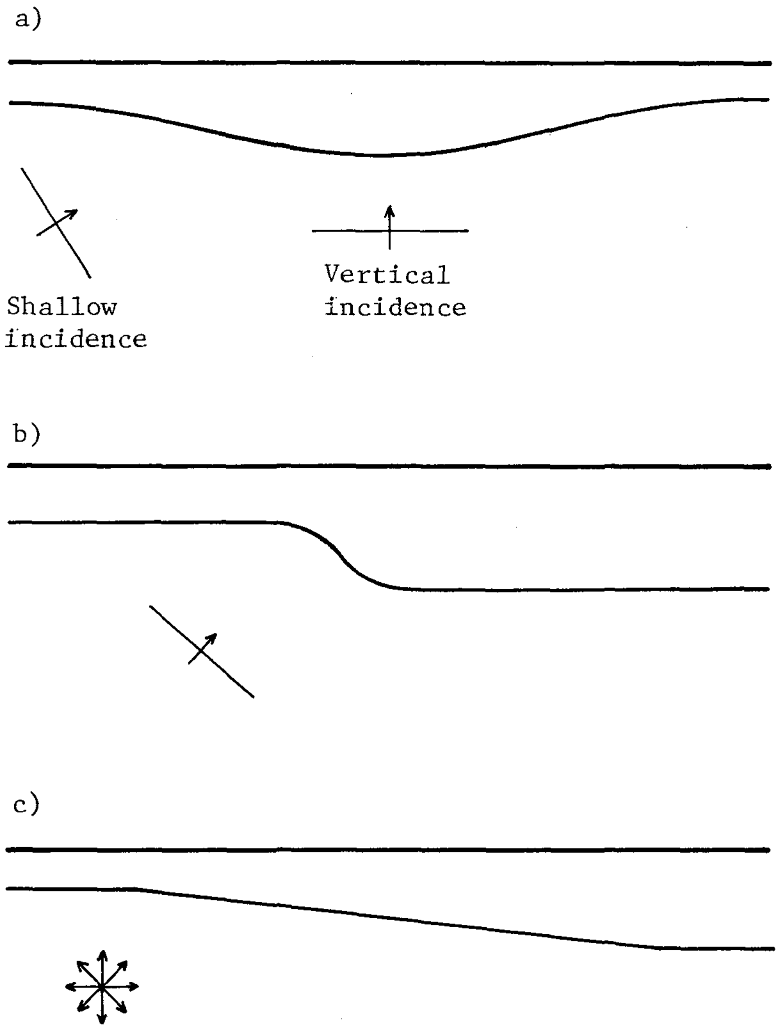
a)
Shallow incidence
Vertical incidence
b)
c)

Figure 2. a) Shallow alluvial basin, A & L (1970).
b) Step in the Moho discontinuity, A & L (1970).
c) Dipping transition layer, H & H (1977).

ments for the irregular Moho interface were due to focusing and defocusing of rays with minor contributions from multiple reflections.

The above analyses were performed essentially in the frequency domain. An analysis of lateral inhomogeneities in the time domain using ray theoretic methods has recently been performed by Hong and Helmberger (1977). They applied generalized ray theory to a dipping transition layer over a halfspace with SH line sources in or below the layer, e.g. Fig. 2c. Diffraction from the corners was neglected and asymptotic approximations used in the Cagniard-de Hoop formalism restricted the input to short-period pulses. The authors calculated a number of surface displacement records for various source positions, dip angles, etc., of use in interpreting surface records in the neighborhood of dipping layers. A useful conclusion was that waves propagating in the downdip direction were more effective in exciting the dipping layer than waves in the updip direction. This was due to the fact that a thickening layer (downdip) tended to decrease the incidence angle of a ray at the interface, rapidly becoming supercritical and trapping the energy, Fig. 3a; whereas a thinning layer (updip) tended to increase the incidence angle and most of the energy leaked into the lower halfspace, Fig. 3b. A second related paper by Hong and Helmberger (1976) dealt with vertically incident SH waves in a soft basin, similar to that treated by Aki and Larner (1970). The analysis was by means of geometrical acoustics. Of primary interest was the focusing and defocusing of waves by the curved interface and the development of caustics. It was noted that foci or caustics near the surface could be significant in terms of earthquake hazards.

In addition to the above investigations, there are many papers dealing with approximate methods for the analysis of wave propagation across surface steps,

a) Downdip propagation

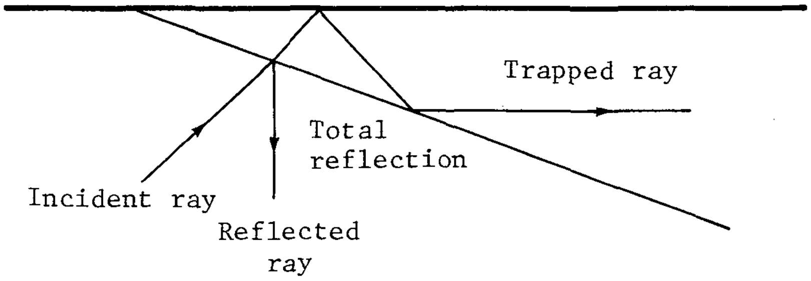
Trapped ray
Total reflection
Incident ray
Reflected ray

b) Updip propagation

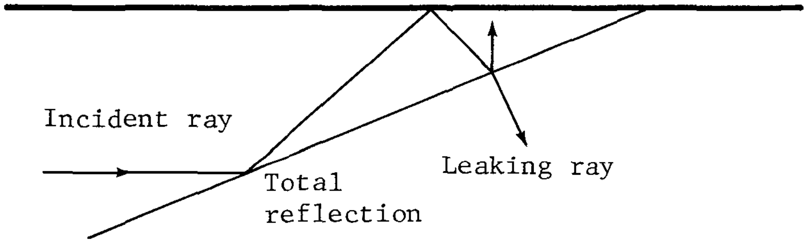
Incident ray
Leaking ray
Total reflection

Figure 3. Comparison between downdip and updip propagation.

nonhorizontally layered structures, etc., e.g. Knopoff and Mal (1967); Alsop et al (1974). The excitation for many of these are surface waves, typically Love waves. Such inputs are motivated by seismological aspects of surface wave propagation across continental margins, e.g. dispersion relations, and are not considered further.

Numerical Modeling Studies

One advantage of exact or approximate analyses over model studies, either numerical or experimental, is the relative ease in which dominant physical mechanisms and phenomena can be isolated. However, in applications model studies are required and this section examines relevant finite difference and finite element solutions.

One of the first extensive numerical studies of lateral inhomogeneities from a seismological viewpoint was a paper by Boore (1970) in which a finite difference code was used to solve the problem of Love waves propagating through a change in crustal thickness. The code used an explicit integration scheme with transient Love wave input by means of initial values over a portion of the grid. It was verified by means of an available exact solution. Surface amplitude and phase information was presented for a transient Love wave with a Ricker wavelet surface displacement incident on a transition in crustal thickness (i.e. depth of Moho discontinuity) from either side. Results obviously applicable to surface motion studies on the scale of interest here were not discussed, however the value of the paper was its presentation of a rigorous numerical approach to the study of such problems, particularly the use of transient inputs and resulting amplitude and phase spectra on the surface. In later papers, Boore looked at the effects of simple topography (hills, valleys and basins) on surface acceleration. An overview of the general approach and various problems examined is given in Boore (1972).

Concurrent with Boore's work was a paper by Lysmer and Drake (1971) on the use of a finite element code to analyze steady state Love wave propagation across nonhorizontally layered structures. Their approach coupled the modal analysis of a horizontally layered input model, a laterally inhomogeneous model and a horizontally layered output model. This is discussed more fully in Lysmer and Drake (1972), where, for input of a fundamental surface wave mode, they were able to compute the fundamental and higher transmitted and reflected modes, accounting exactly for all of the incident energy in terms of surface waves only. One calculation on Love waves in an alluvial basin indicated that most of the surface wave energy propagating across the basin was transmitted at the edge, with negligible reflection. In Drake and Mal (1972) the same method was used to examine Love and Rayleigh waves in the San Fernando Valley. One example showed Love wave surface amplitude amplification by a factor of 5 or so for a shallow dipping layer, as well as considerable lateral variation in displacement. Rayleigh wave amplification was a factor of 2 with less lateral variation. These results were, of course, strongly dependent on input wavelength and layer properties. One apparent discrepancy in the above analysis was that all of the incident surface wave energy was transmitted and reflected as fundamental and higher mode surface waves, whereas, depending on the inhomogeneity, a significant portion should be converted to body waves. However, the results are consistent with the assumption of a fixed boundary at the model base.

In reference to the previously mentioned work of Hong and Helmberger (1977), Hong used a finite element code in his thesis, Hong (1978), to check the results of various ray theoretic approximations. SWIS, a low order explicit scheme developed by Frazier and Peterson (1974) was used. Two problems of interest were the dipping layer excited by an SH line source in the underlying half-space, Fig. 2c, and an alluvial basin excited by a plane SH wave incident vertically from below, Fig. 2a. Because SWIS uses single point spatial integration over an element, Hong investigated the influence of irregular elements at inclined or curved interfaces and element size transitions; no anomalous results were found. The grid size was kept smaller than one-tenth of the quarter-power wavelength in the power spectrum of the source time function. Agreement between ray theoretic and finite element solutions was excellent.

Experimental Modeling Studies

A number of experimental model studies have addressed the problem of wave propagation through laterally inhomogeneous crustal structure. Typically, these deal with seismological effects of the continental margin, e.g. Kuo and Thompson (1967), Martel, et al (1977), and more recently scattering due to topography, e.g. Rogers, et al (1974). Experiments usually consist of laboratory plane stress models with Rayleigh or body waves excited by a small explosive charge or piezoelectric transducer. Note that SH motion, particularly Love waves, are not amenable to such modeling.

A novel experiment in strong motion seismology, on a much larger scale than those above, Wong, et al (1977), used the forced rocking vibration of a nine-story structure at Caltech as a source of SH waves. Thirteen seismometer records were obtained along a 5.5 kilometer array traversing an elongated canyon underlain by a shallow dipping alluvial layer. Subsequent exact analyses of approximate 2-D models of the canyon and dipping layer showed that the dipping layer was considerably more important than the canyon in modifying the records.

An experiment which is particularly relevant to relative motion studies was performed by Stephenson (1973). He showed strong effects of small scale bedrock interface depth variations in generating relative displacements on the surface. The experiment consisted of a stepped bedrock halfspace (modeled by a rigid base) covered by a layer of soil (modeled by jelly). For horizontal bedrock motion normal to the step (provided by a shaker table) relative motion across the step on the surface was large for certain frequencies over distances comparable to the mean depth of soil. Stephenson's explanation was that, for frequencies midway between the resonant frequencies of the soil columns on either side of the step, relative displacement was maximized due to the phase difference. This is a general property of coupled resonators, i.e. one resonator is above resonance and will lag the driving force while the other is below resonance and will lead. Across the coupling the phase lag and lead combine to yield a large relative response. Stephenson concluded that in all probability many damage effects, formerly attributed to local high accelerations or fault movements, are really caused by resonance-induced relative surface displacements.

Field Studies

Detailed field observations are probably the best indicator of the types of lateral inhomogeneities likely to enhance ground response and earthquake damage. The papers described here are to the point but by no means do they represent a complete review.

In an effort to correlate ground response variability with subsurface structure, Murphy and Hewlett (1975) analyzed seismic response in Las Vegas due to six underground nuclear tests at NTS. They found that variations in long-period seismic response of as much as an order of magnitude could be expected at sites only a few kilometers apart. Simple models of surface wave propagation through surface layers of varying thickness could account for much of the observed variability. In addition, surface waves reflected back from the valley boundaries at the base of surrounding mountain ranges were judged to have a significant effect on the response.

Of particular relevance to this review is a paper by Poceski (1969) on the ground effects of the magnitude 6 earthquake in Skopje, Yugoslavia, July 26, 1963. The damage pattern over the small area of the city varied from no damage to complete destruction, separated in exceptional cases by a city street. From subsequent seismic surveys there was generally good correlation between the damage distribution, surface soil thickness and the predominant period of microtremors. However, the greatest destruction occurred on a belt defined by an "abrupt" change of alluvium thickness. Also heavy destruction occurred on the shallow, tapering alluvium side. Cross sections through the most heavily damaged regions are illustrated in Fig. 4. The mechanism by which these inhomogeneities caused such destruction was not well understood.

Discussion

It is clear from the survey that there are a number of geometries and inputs to be included in an investigation of surface response due to lateral inhomogeneity. Two-dimensional representations of the alluvial basin, stepped interface, and dipping transition layer, Fig. 2a-c, are the typical geometries considered, while inputs include the range of common wave types supported by an elastic continuum, e.g. SH body waves and Love and Rayleigh surface waves, with some consideration of P and SV body waves. The survey and this discussion are essentially limited to 2-D phenomena.

In order to categorize and discuss geometrical aspects it is useful to note that the inhomogeneities can be approximated by a combination of uniform

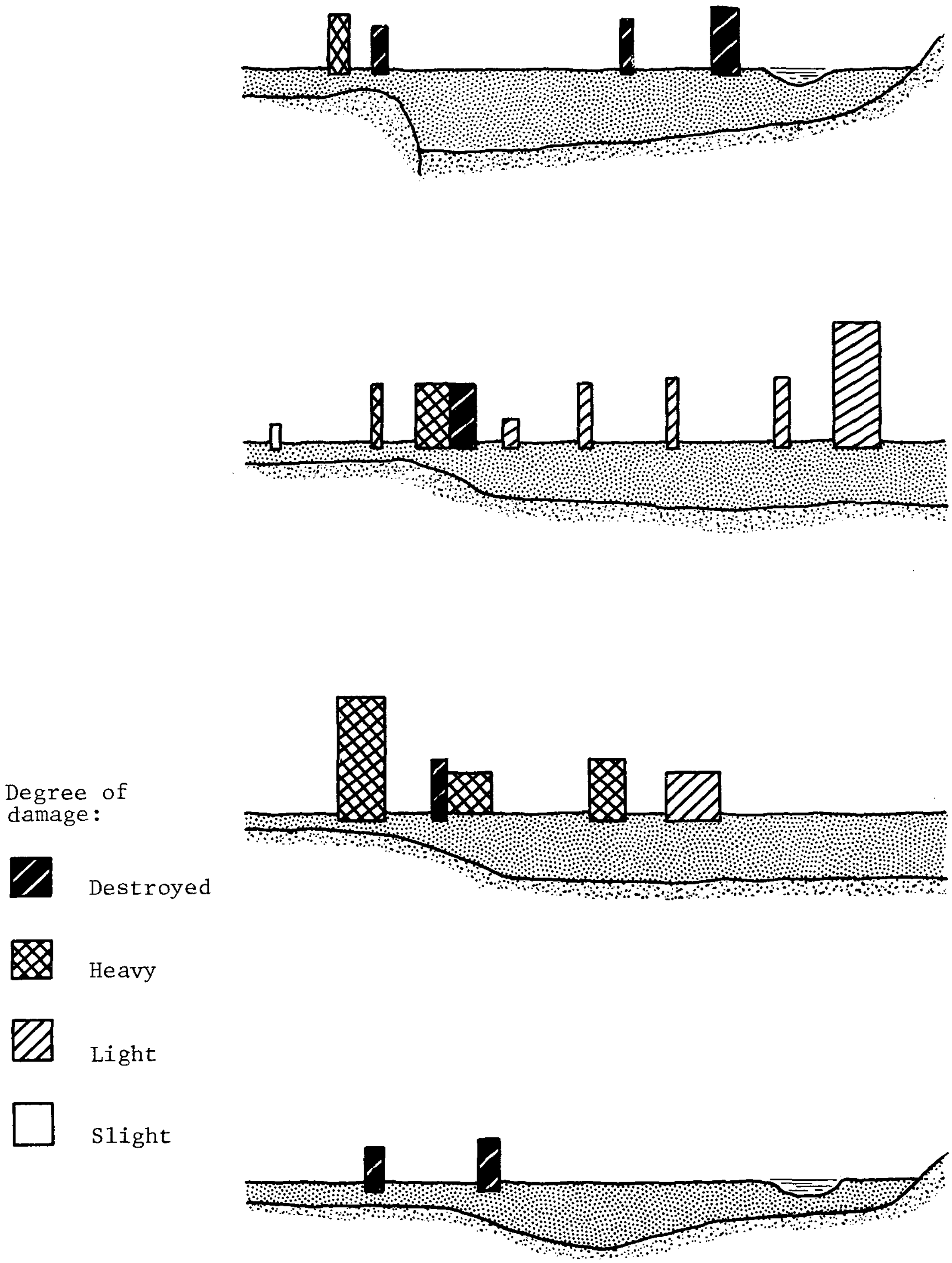
Degree of damage:
Destroyed
Heavy
Light
Slight

Figure 4. Cross sections through the most heavily damaged sections in Skopje (from Poceski (1969)).

surface layers and dipping layers. The transition layer combination shown in Fig. 5a achieves an abrupt or gradual change in depth depending on the choice of parameters. The basin is represented by two transition layers and a uniform layer as in Fig. 5b. In general, the complexity of wave propagation in these structures increases in proportion to the number of characteristic lengths (resonances). The simplest geometry is a degenerate transition layer, namely the surface dipping layer, Fig. 5c, because it does not possess an absolute length scale. Next is the transition layer with from one to three lengths, and then the basin with two to seven lengths.

Just as the complexity of wave propagation depends on the number of characteristic lengths in the geometry, so does it depend on the nature of seismic input. Lengths associated with the input couple with lengths in the geometry to further complicate the response. Plane body waves are the simplest, lacking a length scale due to the source at infinity. When the source moves to a finite distance the length exhibits itself as wavefront curvature. In contrast to the case of body waves, for surface waves excited at an infinite or finite distance, there always appears to be an explicit length associated with depth decay.

Based on the above observations, the most fundamental problem of lateral inhomogeneity is the surface dipping layer, Fig. 5c, subject to plane SH waves incident from below, because both the geometry and input lack a characteristic length. The problems found in the survey are all complicated by numerous lengths, the effects of which are difficult to separate. These are discussed below.

For plane harmonic SH waves incident on a basin at arbitrary angle, it was found in the survey that lateral amplitude variations over the surface were quite pronounced, varying in certain cases by an order of magnitude; and more energy was trapped by grazing incidence than by vertical incidence (W & T (1974),

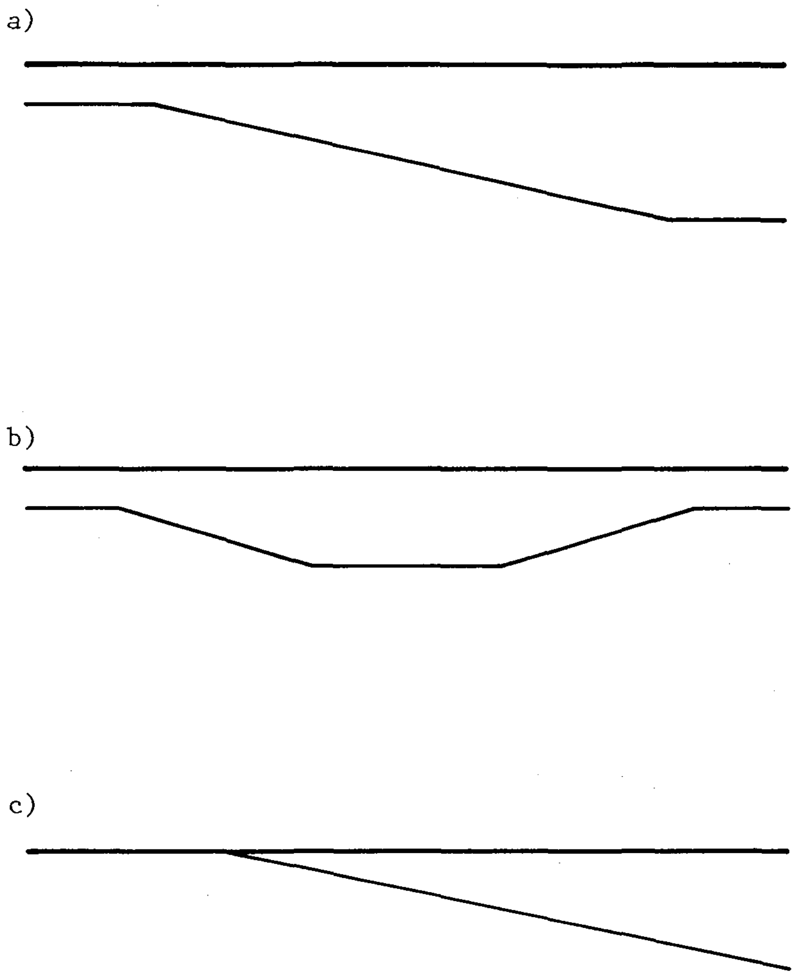

Figure 5.
a) Dipping transition layer.
b) Alluvial basin.
c) Surface dipping layer.

A & L (1970)). The degree to which the high amplitude variations were due to vertical or horizontal interference in the basin was not explored; however, results of H & H (1977) comparing updip and downdip propagation in a transition layer and L & D (1972) on the reflection of surface waves at the edge of a basin indicate that the edges of alluvial basins are poor reflectors. Therefore, it is likely that interference in the horizontal direction (across the basin) is generally less important than that in the vertical. An exception would be the case of high impedance mismatch between the alluvium and adjoining bedrock. This could explain the significant amount of surface wave energy reflected from the base of a mountain range near Las Vegas (M & H (1975)). The observation that grazing incidence was a more effective input than normal incidence can be understood on the basis of critical angles of reflection. For near normal incidence, numerous wave reflections occur between the free surface and interface at subcritical angles (H & H (1978)), leaking much of the energy back into the underlying halfspace; whereas for near grazing incidence the multiple internal reflections more readily become supercritical at the dipping interfaces, thus trapping energy by total internal reflection.

Evidence from the Skopje earthquake (P (1969)) indicates that strong motion enhancement likely to damage conventional structures can occur over an isolated dipping transition layer, Fig. 4. One possible explanation is relative displacement across the transition due to the coupled resonant column effect described in S (1973). However, the transitions in Fig. 4 are typically broader than that assumed by Stephenson, yielding less pronounced gradients of relative motion. Another possibility is near-surface foci or caustics (H & H (1978)) in the transition layer, causing enhanced surface motion. The fact that destruction occurred continuously along a rather nonuniform belt (see Fig. 4 for cross sections) defining a change in alluvium thickness seems to argue against this, however. Also, the calculations of H & H (1977) for pulsed sources in or below such a transition layer give no indication of anomalous surface response. These observations tend to indicate that some other mechanism, beside those found in the literature survey, is responsible for the damage at Skopje.

The problem of lateral inhomogeneity is obviously complicated by the variety and variability of geologic configurations and seismic inputs. As a consequence, the only tools available for solving the general problem are numerical, typically finite element or finite difference modeling procedures. The work of B (1970), L & D (1971) and H (1978) show that this approach is informative and reasonably economical. B (1970) and L & D (1971) used the finite difference and finite element method, respectively, to investigate surface wave propagation through inhomogeneities, while H (1978) used the finite element method as a confirmation of approximate ray theoretic analyses. These methods can be applied to arbitrary geometry and input, and can perform modal or transient (linear or nonlinear) analyses. The transient analysis is well suited to following details of wave propagation in geologic structures, whereas the modal analysis is advantageous when multiple reflections and resonance phenomena predominate. Such methods have well-known limitations related to problem size and spatial/temporal discretization; however these do not detract appreciably from their usefulness as computational tools in modeling surface response of the type discussed above.

Conclusions

The survey shows that our understanding of the effects of near surface lateral inhomogeneity on ground response is qualitative and by no means complete.

For example, 2-D solutions indicate that high amplifications are to be expected in certain alluvial basin configurations, but existing solutions neither explain nor suggest how destructive surface motion can in fact occur over a simple transition in alluvium depth. Clearly some fundamental problems and inputs still need to be examined in order to clarify and bound such phenomena.

A first step is to establish the mechanism whereby lateral inhomogeneities can cause anomalous surface behavior. In the discussion of basin response it was concluded that vertical rather than horizontal interference was the dominant cause of surface amplification. This suggests that the basin edge, modeled as a dipping transition layer, Fig. 5a, be examined for resonance behavior. This also provides a good model of the geology at Skopje, Fig. 4. To allow an analytical rather than numerical solution, the transition layer is further idealized as a surface dipping layer, Fig. 5c, with plane SH waves incident from below. The analysis is performed in Part II of this report.

REFERENCES - PART I

Aki, K. and K. L. Larner (1970). Surface motion of a layered medium having an irregular interface due to incident plane SH waves, J. Geophys. Res. 75, 933-954.

Alsop, L. E., A. S. Goodman and S. Gregersen (1974). Reflection and transmission of inhomogeneous waves with particular application to Rayleigh waves, Bull. Seism. Soc. Am. 64, 1635-1652.

Boore, D. M. (1970). Love waves in nonuniform wave guides: finite difference calculations, J. Geophy. Res. 75, 1512-1527.

Boore, D. M. (1972). Finite difference methods for seismic wave propagation in heterogeneous materials, Methods in Comp. Phys. 11, 1-37.

Drake, L. D. and A. K. Mal (1972). Love and Rayleigh waves in the San Fernando Valley, Bull. Seism. Soc. Am. 62, 1673-1690.

Frazier, G. A. and C. M. Peterson (1974). Three-dimensional stress wave code for Illiac IV, Systems, Science and Software, P. O. Box 1620, La Jolla, Calif., 92037.

Hong, T. L. (1978). Elastic wave propagation in irregular structure, Ph.D. thesis, Seismological Laboratory, Caltech.

Hong, T. L. and D. V. Helmberger (1978). Glorified optics and wave propagation in nonplanar structure, Bull. Seism. Soc. Am. 68, 1313-1330.

Hong, T. L. and D. V. Helmberger (1977). Generalized ray theory for dipping structure, Bull. Seism. Soc. Am. 67, 995-1008.

Knopoff, L. and A. K. Mal (1967). Phase velocity of surface waves in the transition zone of continental margins: 1. Love waves, J. Geophys. Res. 72, 1769-1776.

Kuo, J. T. and G. A. Thompson (1967). Model studies on the effect of a sloping interface on Rayleigh waves, J. Geophys. Res. 68, 6187-6197.

Lysmer, J. and L. D. Drake (1971). The propagation of Love waves across nonhorizontally layered structures, Bull. Seism. Soc. Am. 61, 1233-1251.

Lysmer, J. and L. D. Drake (1972). A finite element method for seismology, Methods in Comp. Phys. 11, 181-216.

Martel, L., M. Munasinghe and G. W. Farnell (1977). Transmission and reflection of Rayleigh wave through a step, Bull. Seism. Soc. Am. 67, 1277-1290.

Murphy, J. R. and R. A. Hewlett (1975). Analysis of seismic response in the city of Las Vegas, Nevada: a preliminary microzonation, Bull. Seism. Soc. Am. 65, 1575-1597.

Poceski, A. (1969). The ground effects of the Skopje July 26, 1963 earthquake, Bull. Seism. Soc. Am. 59, 1-22.

REFERENCES (Continued)

Rogers, A. M., L. J. Katz and T. J. Bennett (1974). Topographic effects on ground motion for incident P waves: a model study, Bull. Seism. Soc. Am. 64, 437-456.

Stephenson, W. R. (1973). A note on elastic relative displacement of soils during earthquakes, Bull. Seism. Soc. Am. 63, 433-440.

Trifunac, M. D. (1971). Surface motion of a semi-cylindrical alluvial valley for incident plane SH waves, Bull. Seism. Soc. Am. 61, 1755-1770.

Wong, H. L. and M. D. Trifunac (1974). Surface motion of a semi-elliptical alluvial valley for incident plane SH waves, Bull. Seism. Soc. Am. 64, 1389-1408.

Wong, H. L., M. D. Trifunac and B. Westermo (1977). Effects of surface and subsurface irregularities on the amplitudes of monochromatic waves, Bull. Seism. Soc. Am. 67, 353-368.

PART II

SURFACE DIPPING LAYER RESPONSE DUE TO INCIDENT PLANE SH WAVES

The lateral inhomogeneity to be investigated in Part II is the surface dipping layer illustrated in Fig. 6 with plane SH waves incident from below. The model consists of two bonded wedges: the acute wedge representing alluvium or sediments, i.e. a soft geologic formation, and the other wedge representing some harder formation. By idealizing these formations as elastic continuua, linear wave propagation techniques can be applied to determine dynamic response. Such methods are particularly simple for wedge-shaped regions with plane wave excitation because no characteristic length exists and solutions exhibit dynamic or self-similarity, e.g. Keller and Blank (1951), Achenbach (1970). In order to simplify the presentation while retaining the important features of the model, the harder wedge is allowed to degenerate to a halfspace as shown in Fig. 6.

In the dipping layer, mass density, shear modulus and shear wavespeed are ρ, μ, $c \equiv \sqrt{\mu/\rho}$, respectively; w is antiplane particle displacement, $\dot{w}$ is particle velocity and $v \equiv \dot{w}/v_o$ is the nondimensionalized velocity, where v_o is a normalization factor. Corresponding quantities in the halfspace are barred, e.g. $\bar{c}$. The input is a plane SH wave incident on the halfspace interface from below, in the downdip direction, with incidence angle, $\bar{\delta}$. This is illustrated in Fig. 7 for a velocity step of amplitude $\bar{v}_o$ so that the nondimensionalized velocity, $\bar{v} \equiv \dot{\bar{w}}/\bar{v}_o$, is equal to 1 behind the step. At $t = 0$ the point of reflection, traveling at $V_o \equiv \bar{c}/\sin\bar{\delta}$, is assumed to pass the edge of the dipping layer. When $t < 0$, to the left of the edge the incident wave reflects in kind off the free surface with amplitude, $\bar{v}_o$ (reflection coefficient, $R = 1$). Behind the reflected wave the particle velocity is therefore $2\bar{v}_o$. As the point of reflection passes the edge, amplitude of the reflected wave changes abruptly from $\bar{v}_o$ to $R\bar{v}_o$, where

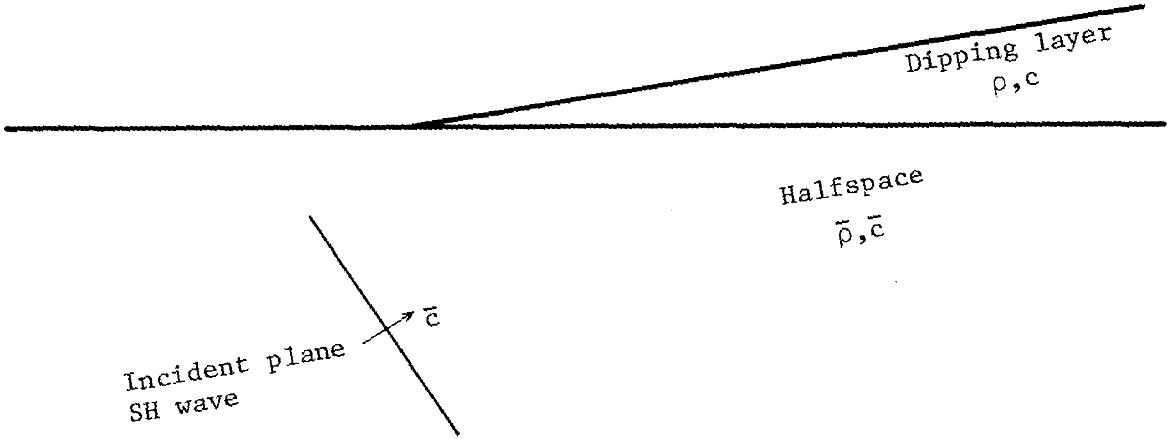
Dipping layer
ρ, c
Halfspace
$\bar{\rho}, \bar{c}$
Incident plane
SH wave
$\bar{c}$

Figure 6. The surface dipping layer problem.

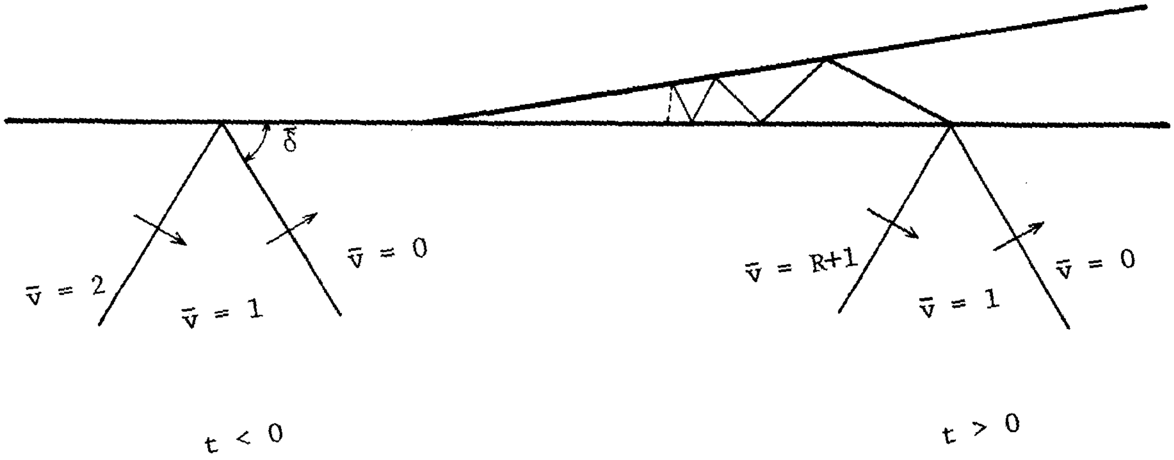
$\bar{\delta}$
$\bar{v} = 2$
$\bar{v} = 1$
$\bar{v} = 0$
$\bar{v} = R+1$
$\bar{v} = 1$
$\bar{v} = 0$
$t < 0$
$t > 0$

Figure 7. The incident and transmitted wave system.

R is the reflection coefficient at the material interface (c.f. (A-11) in Appendix A). In addition there is a diffracted cylindrical wave in the halfspace and layer (not shown) emanating from the edge at t = 0, and a refracted system of plane waves in the dipping layer. Amplitude of the leading refracted, i.e. transmitted, wave is $T\bar{v}_o$, where $T = 1+R$ (A-12).

TIME DOMAIN WEDGE RESPONSE

The coupled system of waves propagating in the dipping layer and halfspace are quite complicated. A complete analysis is possible by applying an integral equation method developed by the author for another type of wedge problem, Wojcik (1977). However, for the purposes of this report a somewhat ad hoc approach is used which yields predominate response as well as considerable physical insight. To this end note that if the impedance ratio,

$$I \equiv \sqrt{\frac{\bar{\rho}\bar{c}}{\rho c}} ,$$

is assumed high (e.g. a low density or slow dipping layer such that $I \gg 1$) then, from results in Appendix A, the incident wave reflects off the material interface as if it were stress free, i.e. $R = 1$. Hence the interface particle velocity is just $2\bar{v}_o$ behind the point of reflection.

The impedance assumption essentially decouples the layer and halfspace and reduces the problem to an elastic wedge with upper surface traction free and prescribed velocity on the lower surface. Solutions are valid for high impedance mismatch across the interface, e.g. alluvium over dense bedrock, and in addition they exhibit the major features of response in the more general case. From this, approximate solutions for moderate impedance mismatch are obtained in a subsequent section.

Self-Similar Solutions

The wedge coordinate system is illustrated in Fig. 8. The equation governing antiplane particle motion, w, is the 2-D wave equation in polar coordinates,

$$w_{rr} + \frac{1}{r} w_r + \frac{1}{r^2} w_{\theta\theta} = \frac{1}{c^2} \ddot{w}. \tag{1}$$

The boundary conditions are

$$\theta = 0: \quad \sigma_{\theta z} = \mu w_\theta \equiv 0 \ , \tag{2a}$$

$$\theta = \gamma: \quad \dot{w} = v_o H(V_o t - r), \tag{2b}$$

where $v_o = 2\bar{v}_o$ is the jump in particle velocity across the point of reflection, which moves at

$$V_o \equiv \bar{c}/\sin \bar{\delta} \ . \tag{3}$$

Because no characteristic length appears in the problem, dimensional analysis yields the following nondimensional groups

$$v \equiv \frac{\dot{w}}{v_o} \ , \quad s \equiv \frac{ct}{r} \ , \ \theta \ ,$$

to which solutions must conform. The particle velocity is therefore self-similar, i.e. snapshots of the velocity field at increasing times are always similar and the spatial metric scales linearly with time.

In terms of the nondimensional particle velocity, v, and similarity variable, s, the governing wave equation becomes

$$(s^2-1)\ v_{ss} + s v_s + v_{\theta\theta} = 0, \tag{4}$$

(i.e. taking the time derivative of (1), dividing by v_o and changing variables via $t v_t = -r v_r = s v_s$ for v a function of s and θ only). The boundary conditions become

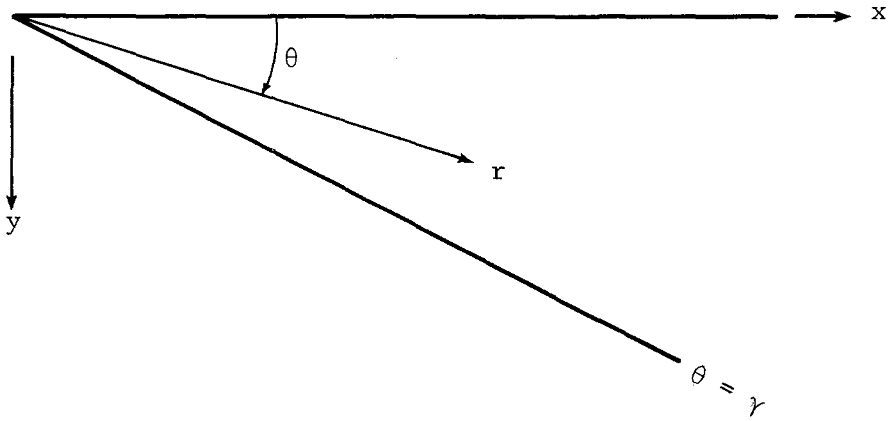

Figure 8. The wedge coordinate system.

$$\theta = 0: \quad v_\theta = 0 \; , \tag{5}$$

$$\theta = \gamma: \quad v = H(s-c/V_o) \; . \tag{6}$$

The resulting differential equation is of mixed hyperbolic-elliptic type. For $s > 1$ the transformation, $p \equiv \cosh^{-1}s$, reduces it to canonical-elliptic form (Laplace's equation),

$$v_{pp} + v_{\theta\theta} = 0 \; , \tag{7}$$

while for $|s| < 1$, $q \equiv \cos^{-1}s$ yields the canonical-hyperbolic form (one-dimensional wave equation),

$$v_{qq} = v_{\theta\theta} \; . \tag{8}$$

In the hyperbolic domain, $|s| < 1$, d'Alembert's solution of the wave equation is

$$\begin{aligned} v &= V_+(\alpha_+) + V_-(\alpha_-) \; , \\ \alpha_\pm &= \theta \pm \cos^{-1}s \; , \end{aligned} \tag{9}$$

where $\alpha_\pm$ are characteristic coordinates, constant on straight lines tangent to the diffracted wavefront, $r = ct$ (i.e. $s = 1$, also a characteristic), at $\theta_c = \alpha_\pm$, Fig. 9. The solution in the elliptic domain, $s > 1$, can be written as

$$\begin{aligned} v &= \text{Re } V(\alpha) \; , \\ \alpha &= \theta + i \cosh^{-1}s \; , \end{aligned} \tag{10}$$

where $V(\alpha)$ is an analytic function of the complex variable, α, over a semi-infinite strip in the α plane, Fig. 10.

Plane Wave Solutions in the Hyperbolic Domain

Plane wave solutions in the hyperbolic domain are dervied in Appendix B. They consist of multiply reflected plane jumps in particle velocity propagating between the wedge faces as shown in Fig. 11. The discontinuities of course co-

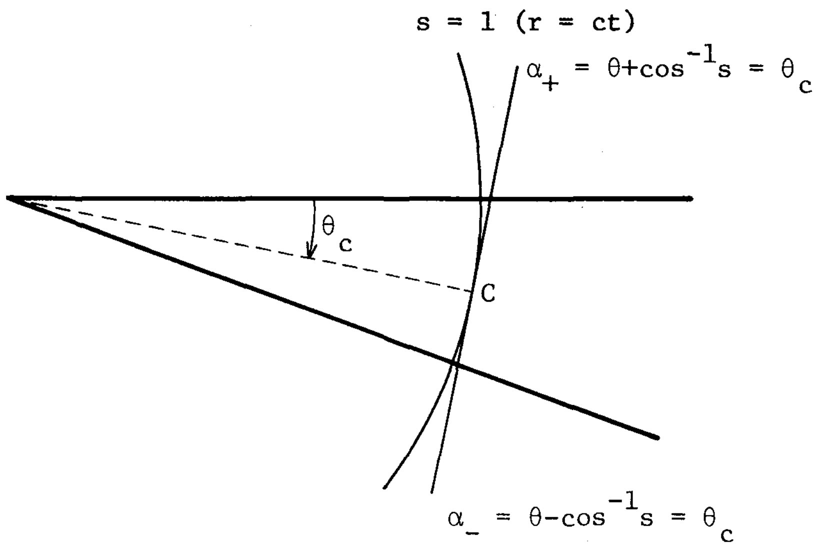

$s = 1$ $(r = ct)$
$\alpha_+ = \theta + \cos^{-1}s = \theta_c$
θ_c
C
$\alpha_- = \theta - \cos^{-1}s = \theta_c$

Figure 9. Characteristics in the hyperbolic domain.

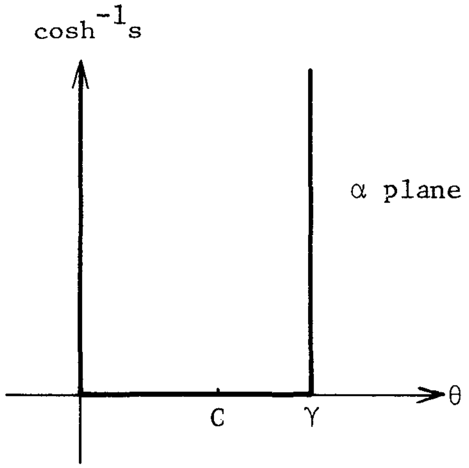

$\cosh^{-1}s$
α plane
θ
C
γ

Figure 10. Semi-infinite strip in the complex α plane.

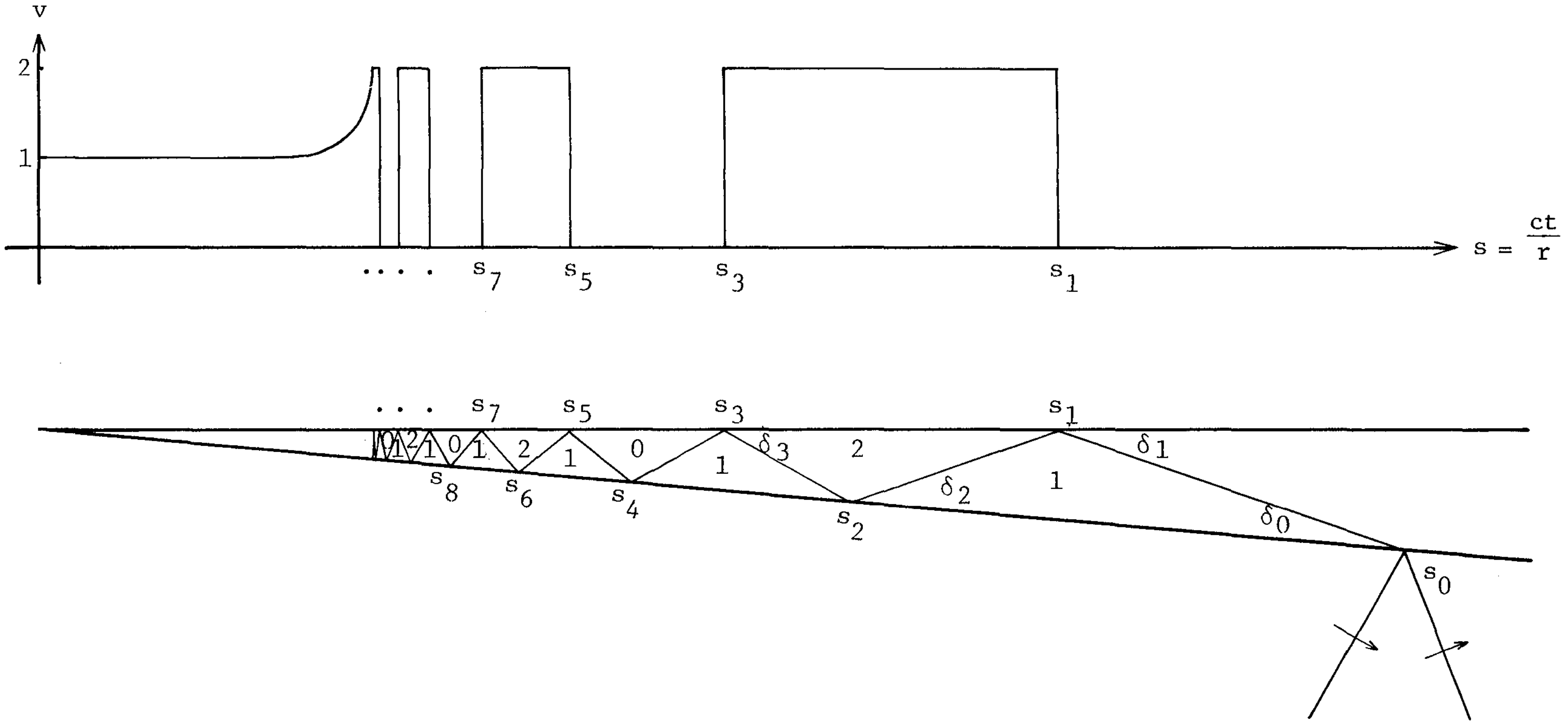
v
2
1
s = ct/r
. . . .
s7
s5
s3
s1
. . .
s7
s5
s3
s1
δ1
δ3
2
1
0
1
2
1
0
1
2
δ2
1
δ0
s8
s6
s4
s2
s0

Figure 11. Plane wave solutions in the hyperbolic domain and surface response including the diffracted wave.

incide with the $\alpha_{\pm}$ characteristics. The points of reflection are at

$$s_n = \sin\delta_n \ , \tag{11}$$

where δ_n is the angle of incidence and reflection,

$$\delta_n = n\gamma + \delta_0 \ , \tag{12}$$

with

$$\delta_0 = \sin^{-1} s_0 \ , \tag{13}$$

being the angle of refraction of the initial wave due to the jump in particle velocity at $s_0 \equiv \frac{c}{V_o}$. From (A-11) the reflection coefficient off a free boundary is +1, while off a rigid boundary it is -1. Therefore across the wave between s_0 and s_1 (denoted by s_0s_1) the normalized velocity increases by one and likewise across s_1s_2; and across s_2s_3 and s_3s_4 it decreases by one. The resulting velocity field is indicated in the figure. The free surface response is plotted above the wedge and it is seen that the incident step is converted to a number of pulses of magnitude 2 propagating away from the wedge vertex. This surface response can be written as

$$v(s) = 2 \sum_{n=1}^{J} (-1)^{n+1} H(s-s_{2n-1}) \ , \tag{14}$$

where J is the number of internal reflection off the free surface (c.f. (B-9) in Appendix B).

Diffracted Solutions in the Elliptic Domain

Diffracted solutions in the elliptic domain are derived in Appendix C. Physically these correspond to either a loading or unloading wave from the vertex which provides the transition between the dynamic response in the hyperbolic domain, i.e. the plane wave solution, and the long-time response at the vertex, where $v = 1$. The solution for $V(\alpha)$, from which particle velocity, v, is obtained as the real part, is found by mapping the semi-infinite strip in the α plane, Fig. 10, onto a halfplane and constructing a solution by means of analytic function theory. The result of this procedure is a solution for v_s, which on the free surface is

$$v_s(s) = \frac{(-1)^J}{\gamma} \frac{\sin\frac{\pi\theta_c}{\gamma}}{\sqrt{1+\cos\frac{\pi\theta_c}{\gamma}}} \cdot \frac{1}{\sqrt{s^2-1}} \frac{\sqrt{1+\cosh(\frac{\pi}{\gamma}\cosh^{-1}s)}}{\cosh(\frac{\pi}{\gamma}\cosh^{-1}s)-\cos\frac{\pi\theta_c}{\gamma}} . \qquad (15)$$

Note that this is singular but integrable at $s = 1$ due to the wavefront singularity, $1/\sqrt{s^2-1}$. The critical angle, θ_c, is the angle at which the plane wave solution terminates tangentially on the $s = 1$ diffracted cylindrical wave, and is given by (B-10). When $\theta_c = 0$, v_s vanishes for $s > 1$ and the surface velocity is constant, equal to unity behind the diffracted front. Otherwise the velocity approaches unity as shown in Fig. 11 where the behavior of v near $s = 1^+$ is like $\sqrt{s-1}$.

Time Domain Response Spectra

It has been shown, (14), that a step in velocity on the lower surface of the wedge is converted to a number of pulses on the free surface. There are typically two approaches used in analyzing such time domain motion, one physical and the other mathematical. Because ultimate interest is in the response of physical systems located on the wedge surface, the physical characterization is in terms of the response of an array of single degree of freedom oscillators to the surface motion covering the frequency window of interest. This yields the so-called response spectrum. The mathematical characterization is by means of the Fourier transform and resulting amplitude and phase spectra. The mathematical method of Fourier analysis is more general and is therefore applied in the following sections.

FREQUENCY DOMAIN WEDGE RESPONSE

The surface response has been determined for a simple jump, v_o, in particle velocity, corresponding to a delta function in acceleration (multiplied by v_o), traveling on the lower surface. In general, knowing the response to a delta function acceleration input, call it a_R^δ, then applying the superposition principle, the response to arbitrary acceleration input, a_I, follows from the convolution integral,

$$a_R = \int_0^t a_I(t-\tau)\; a_R^\delta(\tau)\,d\tau \quad . \qquad (16)$$

For harmonic input, if a_I is $\omega\cos\omega t$, corresponding to $v_I = \sin\omega t$, then

$$a_R = \omega \left[\cos\omega t \int_0^t \cos\omega\tau \; a_R^\delta(\tau)\,d\tau + \sin\omega t \int_0^t \sin\omega\tau \; a_R^\delta(\tau)\,d\tau \right] .$$

Steady state response is found by replacing t with $t + 2n\pi/\omega$ for $n \to \infty$ through the integers. This yields

$$a_R = \omega\, A \cos(\omega t - P) \; , \qquad (17)$$

where A is the amplitude of the Fourier transform of a_R^δ, and P is the corresponding phase, i.e.

$$\tilde{a}_R^\delta \equiv \int_0^\infty e^{i\omega t} \; a_R^\delta(t)\,dt \; , \qquad (18)$$

$$A(\omega) = \mathrm{Mod}\; \tilde{a}_R^\delta \quad , \quad P(\omega) = \mathrm{Arg}\; \tilde{a}_R^\delta \; .$$

Note that $a_R^\delta \equiv 0$ for $t < 0$.

To calculate harmonic surface response first note that surface acceleration, $w_{tt} = v_o v_t$, can be expressed as

$$w_{tt} = \frac{cv_o}{r} v_s$$

by virtue of the self-similarity (i.e. $t\, v_t = s\, v_s$). The surface response due to a delta function in acceleration across the input wave is w_{tt}/v_o, hence

$$a_R^{\delta} = \frac{c}{r} v_s \ ,$$

and substituting this into the Fourier transform gives

$$\tilde{a}_R^{\delta} = \int_o^{\infty} e^{i\Omega s}\, v_s(s)\,ds \quad , \qquad (19)$$

where Ω is the nondimensional frequency parameter, $\Omega \equiv \frac{r\omega}{c}$.

In the hyperbolic domain, $0 < s < 1$, differentiating (14) gives

$$v_s = 2 \sum_{n=1}^{J} (-1)^{n+1}\, \delta(s - s_{2n-1}) \qquad (20)$$

from which (19) is evaluated directly, using the sifting property of the delta function, as

$$\tilde{a}_R^{\delta}\Big|_{\text{plane waves}} = 2\sum_{n=1}^{J} (-1)^{n+1}\, e^{i\Omega s_{2n-1}} \qquad (21)$$

This gives the contribution of the multiply reflected plane waves.

In the elliptic domain, $s > 1$, substituting (15) directly into (19) and integrating from 1 to ∞ yields the Fourier transform of the surface acceleration due to the diffracted wave. Numerical evaluation of the singular Fourier integral is a simple exercise if the integrand is rewritten as

$$\tilde{a}_R^{\delta}\Big|_{\text{diffracted wave}} = \frac{(-1)^J}{\gamma} \frac{\sin\frac{\pi\theta_c}{\gamma}}{\sqrt{1+\cos\frac{\pi\theta_c}{\gamma}}} \int_o^{\infty} e^{i\Omega \cosh p}\, \frac{\sqrt{1+\cosh\frac{\pi p}{\gamma}}}{\cosh\frac{\pi p}{\gamma} - \cos\frac{\pi\theta_c}{\gamma}}\, dp \qquad (22)$$

where $p \equiv \cosh^{-1} s$ and $dp = ds/\sqrt{s^2-1}$. The integrand decays like $e^{-\frac{\pi p}{2\gamma}}$ for moderate p, hence for wedge angles of interest here (on the order of 10° or less, such that $\frac{\pi}{2\gamma} \geq 9$) the range of integration is typically less than 2. For large Ω the integrand is highly oscillatory and an asymptotic representation of the Fourier transform can be obtained using the method of stationary phase, e.g. Copson (1967). Noting that the phase, $\Omega \cosh p$, in (22) is stationary at the lower limit, it follows that

$$\tilde{a}^{\delta}_{R}\Big|_{\text{diffracted wave}} \sim \frac{(-1)^{J}}{\gamma} \frac{\sin\frac{\pi\theta_c}{\gamma}}{\sqrt{1+\cos\frac{\pi\theta_c}{\gamma}}} \left[\frac{\sqrt{\pi/\Omega}}{1-\cos\frac{\pi\theta_c}{\gamma}} e^{i(\Omega+\pi/4)} \right] . \qquad (23)$$

Therefore the Fourier transform, hence the contribution of the diffracted wave, decays like $1/\sqrt{\Omega}$ for Ω large. Because $\Omega = \frac{r\omega}{c}$ this is equivalent to a decay like $1/\sqrt{r}$ for fixed ω, or $1/\sqrt{\omega}$ for fixed r.

Summing the Fourier transforms of the hyperbolic and elliptic surface response and calculating the amplitude and phase spectra, $A(\omega)$ and $P(\omega)$ respectively, the harmonic velocity and displacement response are

$$v = A(\omega) \sin(\omega t - P(\omega)), \qquad (24)$$

$$d = \frac{-1}{\omega} A(\omega) \cos(\omega t - P(\omega)), \qquad (25)$$

i.e. integrating (17). The actual velocity and displacement follow a multiplication by v_o. Representative amplitude and phase spectra versus Ω are plotted in Figs. 12 and 13 respectively, for a range of wedge angles with $V_o = 3c$. The nondimensional frequency, $\Omega = \frac{r\omega}{c} = 2\pi\frac{r}{\lambda}$, where λ is the wavelength in the wedge, can be viewed as either a space-fixed or frequency-fixed coordinate. For example, Fig. 12 can be interpreted as the amplitude at some fixed distance, r, from the vertex for a range of input frequencies; or conversely, as the amplitude versus distance for a fixed frequency. The latter interpretation is assumed in what follows.

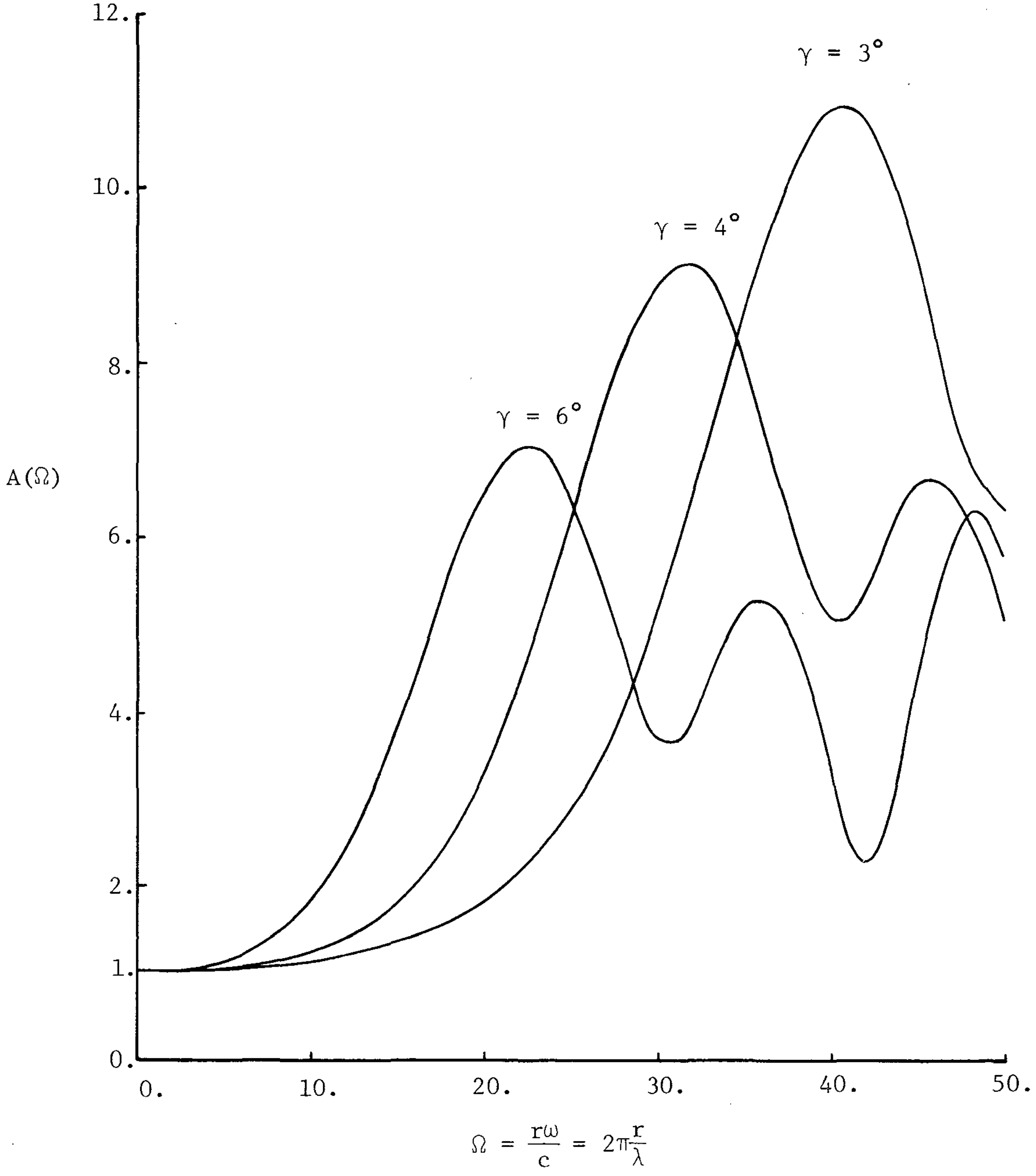

Figure 12. The normalized velocity amplitude spectrum for various wedge angles, with $V_o = 3c$.

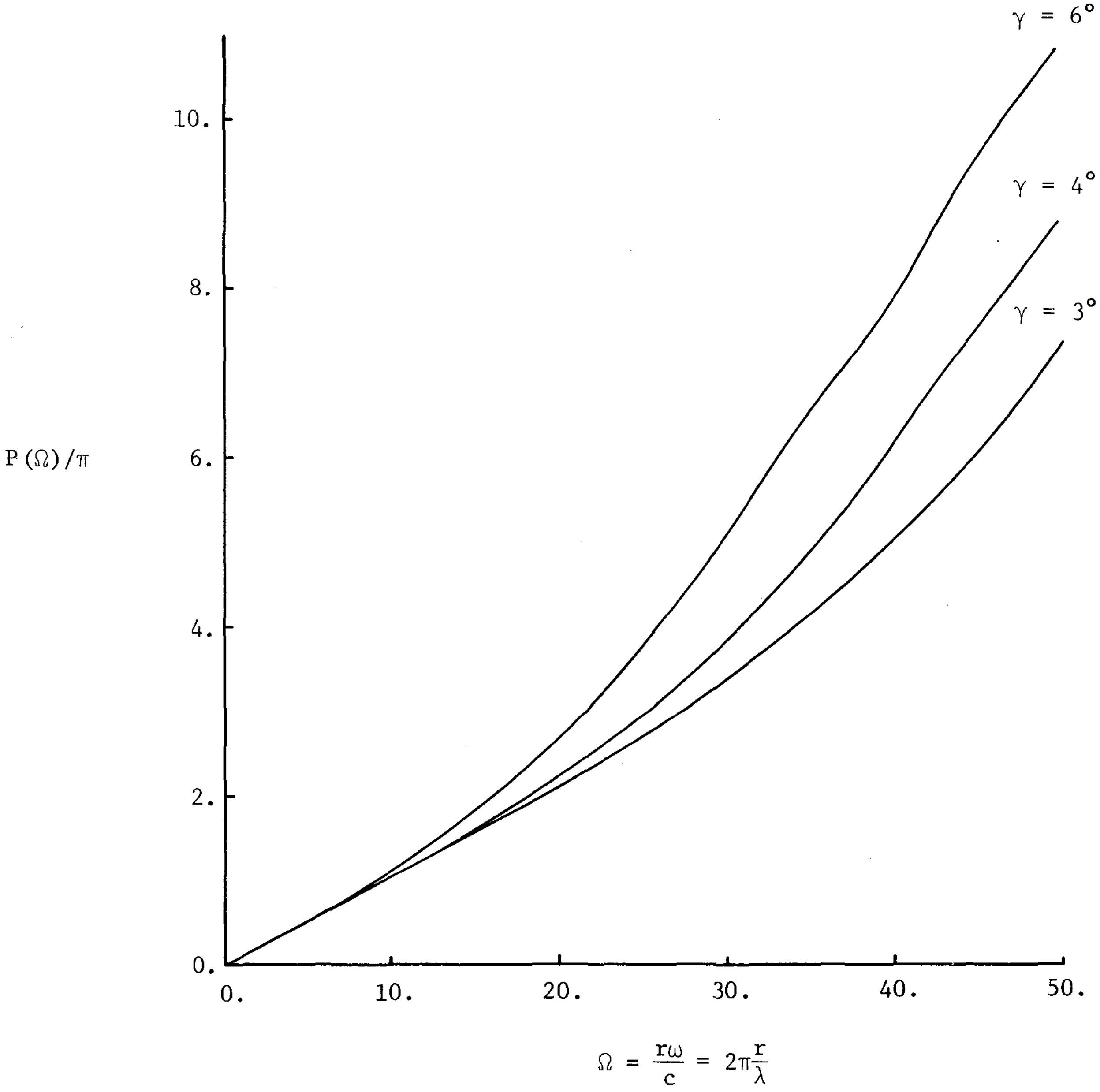

Figure 13. The normalized velocity phase spectrum for various wedge angles, with $V_o = 3c$.

The Amplitude Spectrum: Translational Surface Motion

The principal feature of the amplitude spectrum is the pronounced peak in surface response. On a 3^o wedge, for example, there is an order of magnitude amplification at $\Omega = 2\pi\frac{r}{\lambda} \simeq 40$, i.e. at a distance from the vertex of approximately 6.4 wavelengths for a fixed input frequency. The magnitude of the amplification and the frequency at which it occurs are of course dependent on the wedge angle and phase velocity, V_o, of the input on the lower face. This dependence is illustrated in Fig. 14. The amplitude increases as the wedge angle decreases and as V_o increases.

The mechanism for the surface velocity amplification is constructive interference of outgoing waves from the edge. The harmonic contribution of the diffracted wave is a single wavetrain of amplitude 1 or less, while the contribution of the multiply reflected plane waves is a wavetrain of magnitude 2 for each of the J free surface reflections. Clearly, the more internal reflections the higher the amplification when the resulting harmonic waves are in phase. From results derived in Appendix B, the number of free surface reflections behaves like

$$\text{Int}\left(\frac{\cos^{-1} c/V_o}{2\gamma}\right),$$

where Int( ) gives the integral part of the argument. Hence, in a number-theoretic sense J is inversely proportional to γ and increases with V_o, in qualitative agreement with the results plotted.

In Fig. 15 the amplitude spectrum is plotted with and without the diffracted wave. It is seen that the diffracted part is significant in the lower frequencies, but at higher frequencies, where the high amplifications occur, its effect

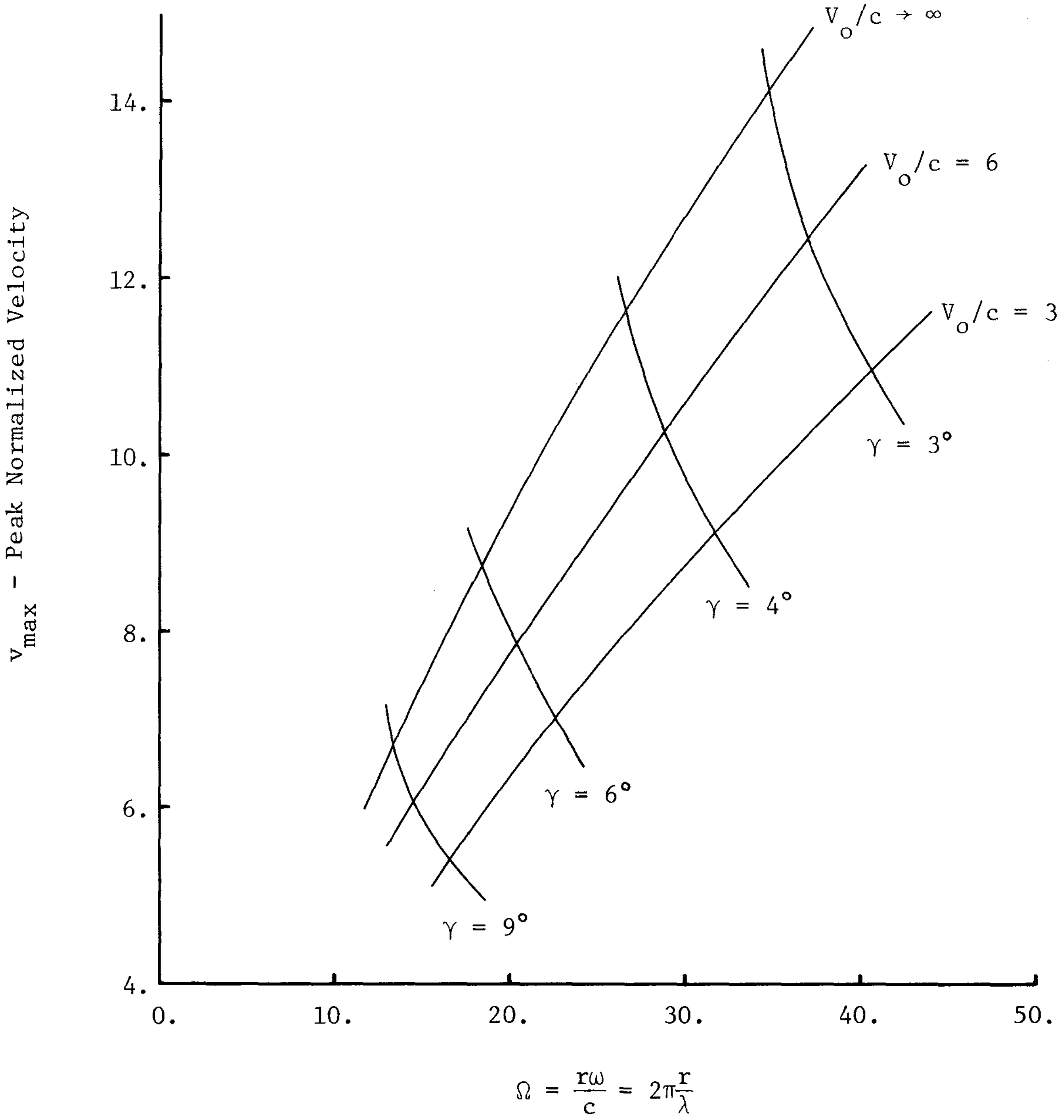

Figure 14. Peak normalized velocity for a range of wedge angles, γ, and interface phase velocities, V_o.

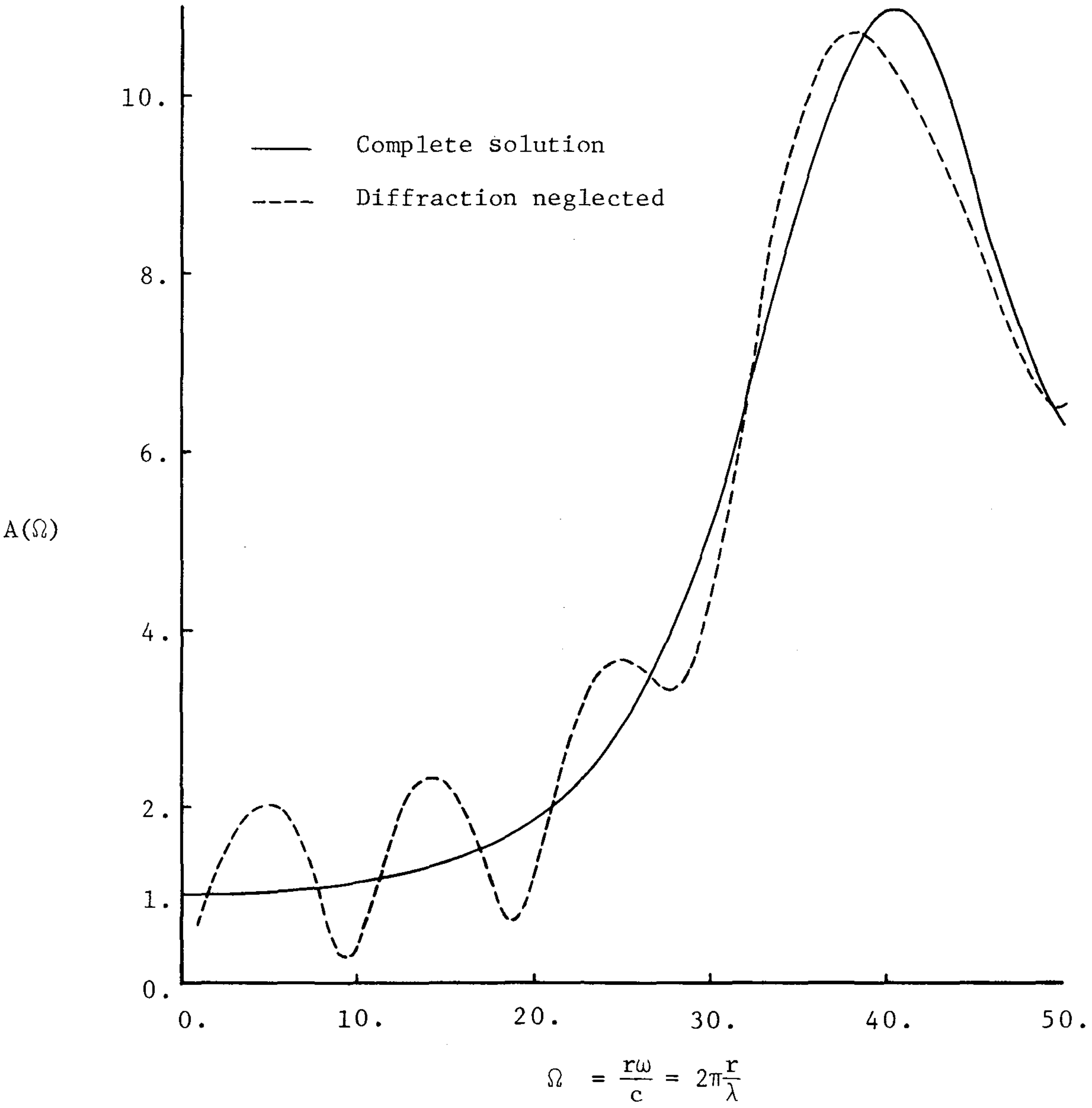

Figure 15. A representative velocity amplitude spectrum with and without the diffracted wave ($\gamma = 3°$, $V_o = 3c$).

is diminished by the $\sqrt{1/\Omega}$ decay, (23). In Fig. 16 the spectrum for a higher frequency range is shown. Clearly the first spectral peak, from which Fig. 14 was obtained, is not necessarily the highest. Each peak corresponds to constructive interference of the outgoing wavetrains, and this type of behavior continues to infinity.

The Phase Spectrum: Rotational and Relative Surface Motion

The role of the phase spectrum is, in conjunction with the amplitude spectrum, to determine surface rotation (at a point) and relative surface motion between spatially separated points. Referring to Fig. 13, the phase is an increasing, reasonably smooth function of frequency, Ω.

Motion at a point on the surface is composed of a translational component, discussed in the previous section, and a rotational component. Infinitesimal rotation, denoted by ψ, is equal to the limit of $\frac{\Delta d}{\Delta r}$ as $\Delta r \to 0$, e.g. the inset in Fig. 17. Differentiating (25), noting that $\frac{\partial}{\partial r} = \frac{\omega}{c}\frac{\partial}{\partial \Omega}$, and rearranging yields

$$\psi = \frac{1}{c}\sqrt{A'^2+A^2P'^2}\,\sin\left(\omega t-\tan^{-1}\frac{AP'\sin P-A'\cos P}{AP'\sin P+A'\cos P}\right), \qquad (26)$$

where the prime designates a derivative with respect to Ω. This is normalized by multiplying by V_o, whence $V_o\psi$ is the ratio of surface rotation to interface rotation, i.e. the rotation output, divided by the rotation input. The phase of rotation in (26) is of no interest here. The normalized rotation amplitude spectrum,

$$A_R \equiv \frac{V_o}{c}\sqrt{A'^2+A^2P'^2}, \qquad (27)$$

is plotted in Fig. 17, corresponding to the spectra in Figs. 12 and 13. The peak normalized rotation for a range of wedge angles and interface phase velo-

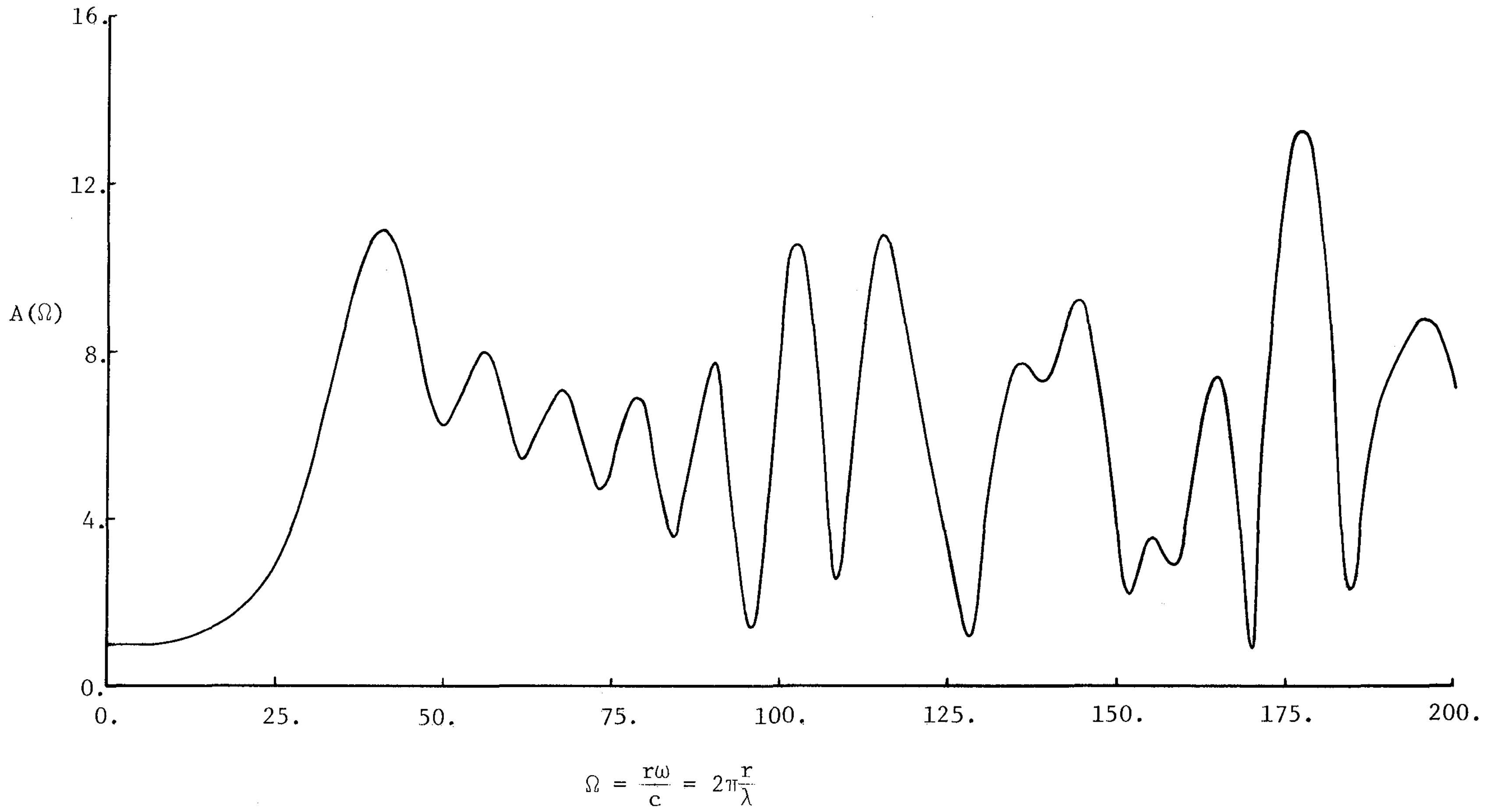

Figure 16. A representative amplitude spectrum in the higher frequency range ($\gamma = 3°$, $V_o = 3c$).

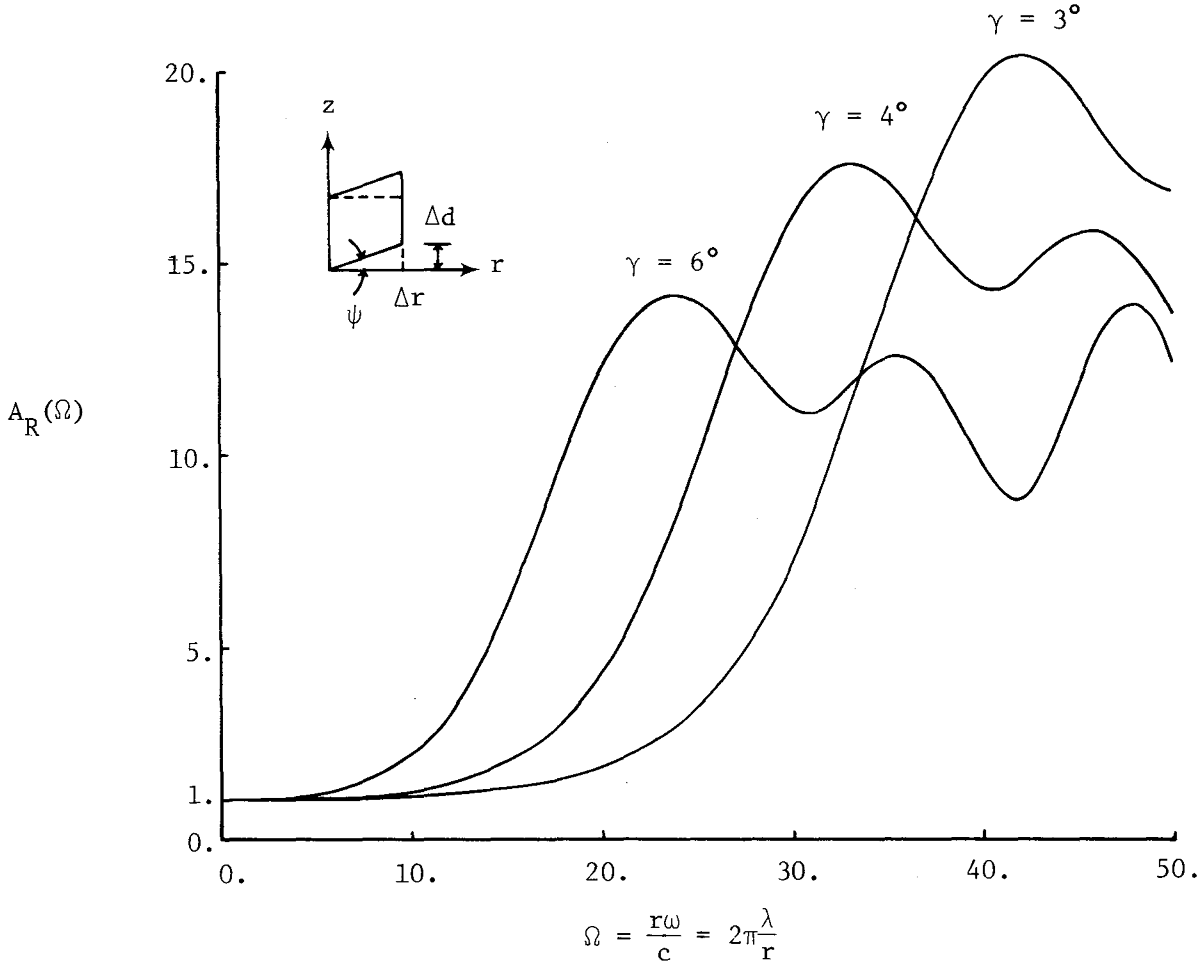

Figure 17. The normalized rotation amplitude spectrum for various wedge angles, with $V_o = 3c$ (note, $\psi = A_R/V_o$).

cities is plotted in Fig. 18. It is apparent that the wedge is an efficient amplifier of rotational motion. Note however, that for cases with high amplification, e.g. $V_o/c = 9$, the input motion is correspondingly less; therefore the actual surface motion does not depend on V_o to the degree the normalized results would indicate.

In order to evaluate the dependence of surface rotation on diffraction, a rotation amplitude spectrum with and without the diffracted wave is shown in Fig. 19. A similar plot of the derivative of the velocity phase spectrum used in (27) is shown in Fig. 20. Clearly, for the higher frequencies where high amplification occurs, diffraction is a minor contributor.

Over distances on the surface much shorter than the incident wavelength, the translational and rotational components described above are sufficient to characterize surface response. However, between points separated by some fraction of a wavelength, relative motion is important. Consider two stations, 1 and 2, on the surface of the wedge, e.g. the inset in Fig. 21, separated by a so-called gagelength, $L = r_2 - r_1$. Relative velocity, Δv, between the two stations is

$$\Delta v = A_1 \sin(\omega t - P_1) - A_2 \sin(\omega t - P_2) \;,$$

where the As and Ps are evaluated at each station, e.g. $A_2 = A(\Omega_2) = A(2\pi\frac{R+L}{\lambda})$. This can be written as

$$\Delta v = \Delta A \sin(\omega t - \Delta P), \tag{28}$$

with ΔA given by (the law of cosines)

$$\Delta A = \sqrt{A_1^2 + A_2^2 - 2A_1A_2\cos(P_1 - P_2)} \;. \tag{29}$$

Clearly ΔA is maximum, equal to $A_1 + A_2$, when the phase difference is an odd

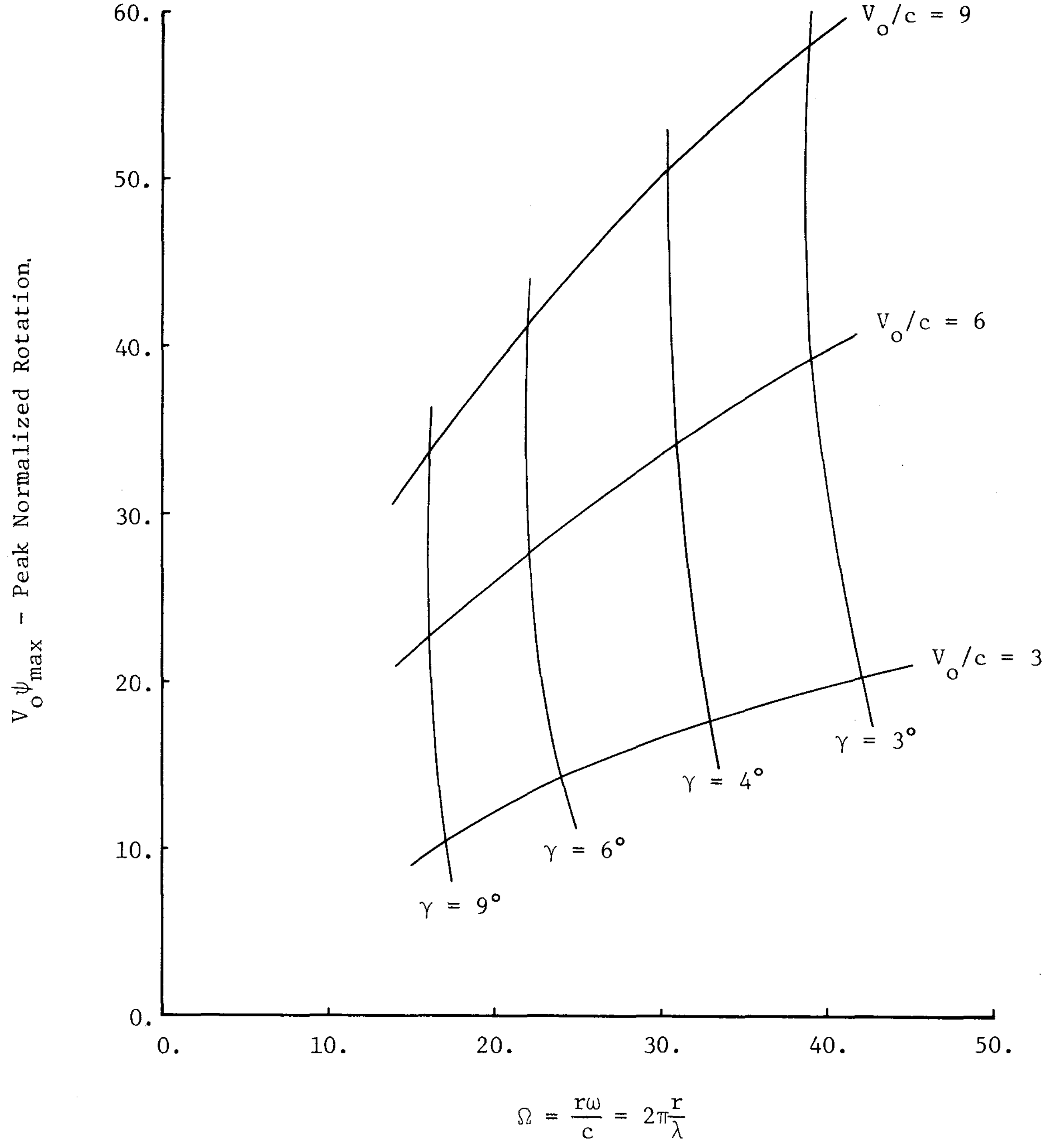

Figure 18. Peak normalized rotation for a range of wedge angles, γ, and interface phase velocities, V_o.

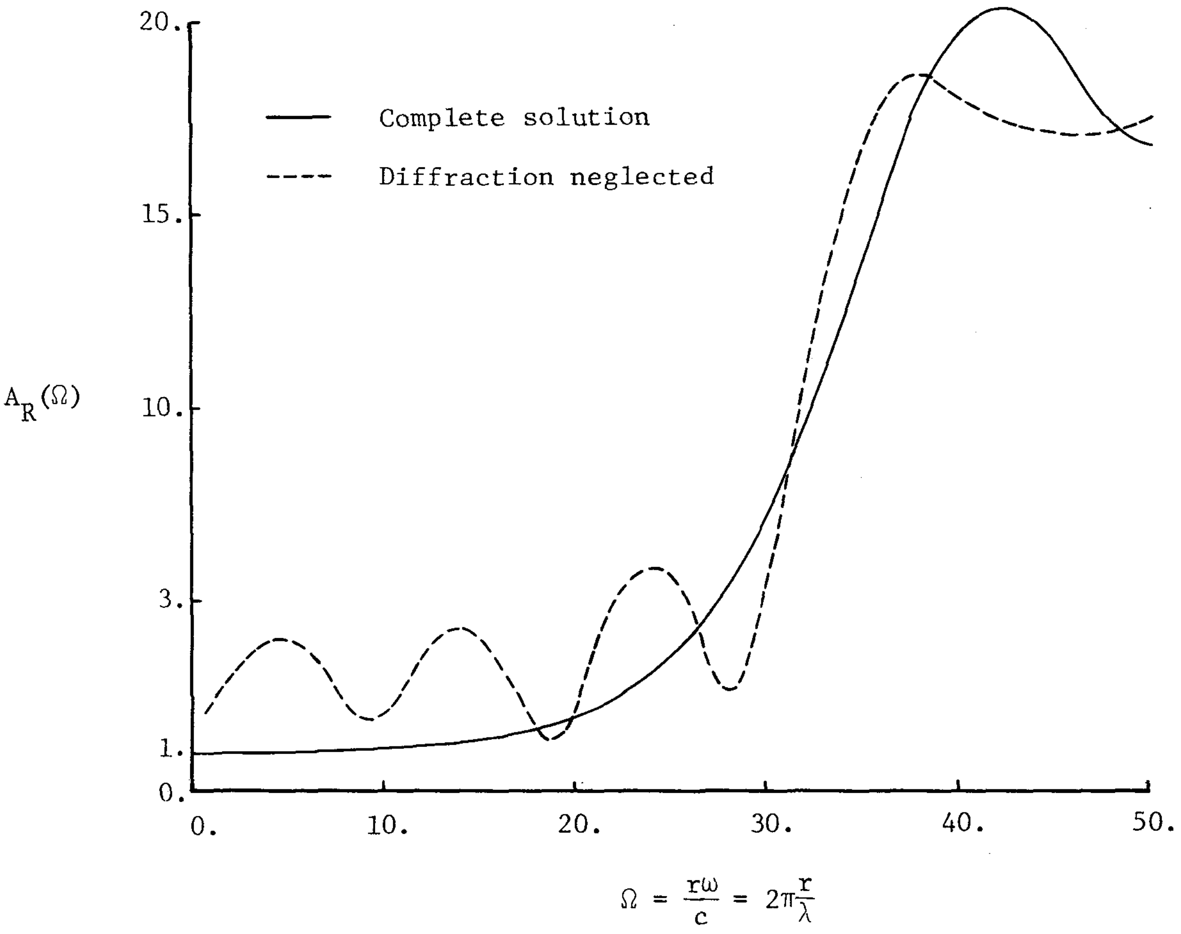

Figure 19. A representative rotation amplitude spectrum with and without the diffracted wave ($\gamma = 3°$, $V_o = 3c$).

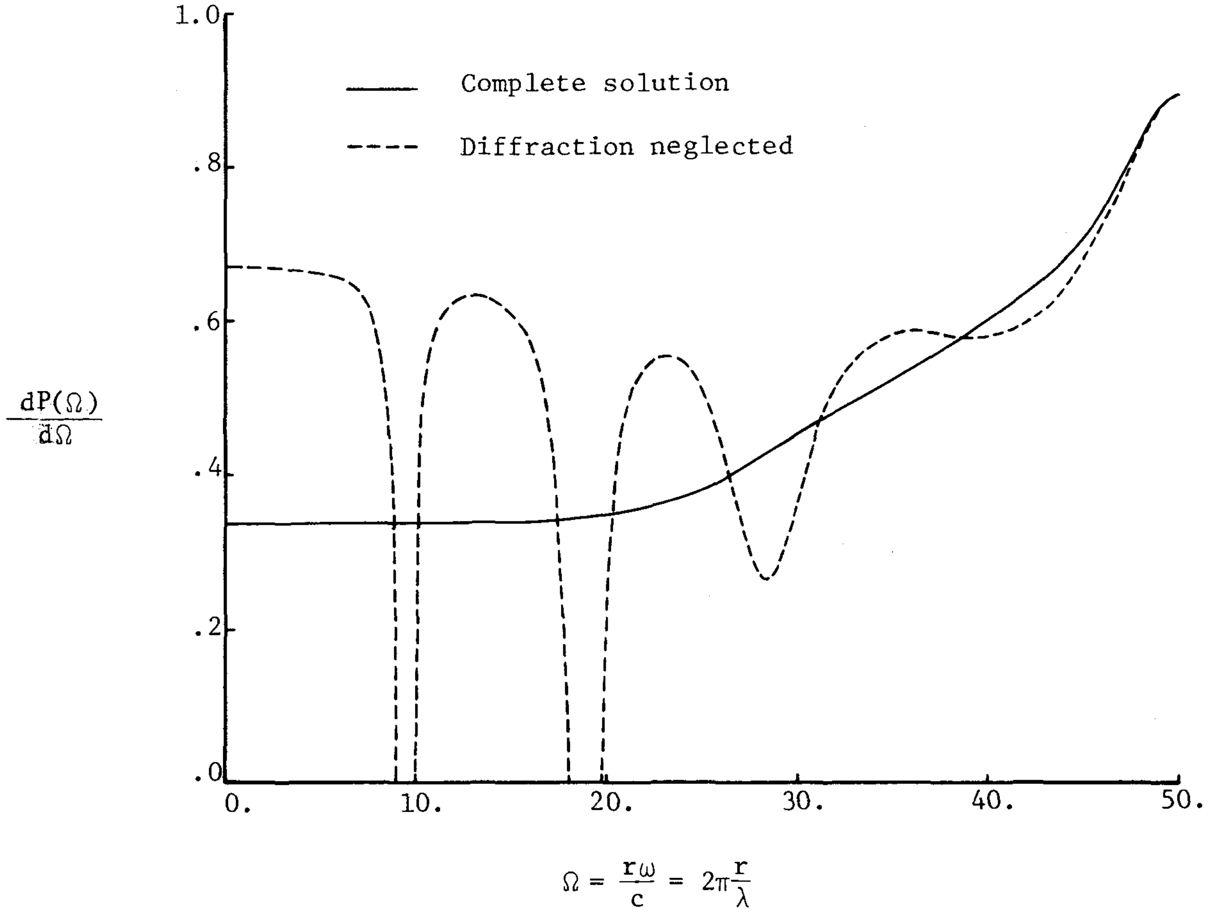

Figure 20. A representative velocity phase spectrum derivative with and without the diffracted wave ($\gamma = 3°$, $V_o = 3c$).

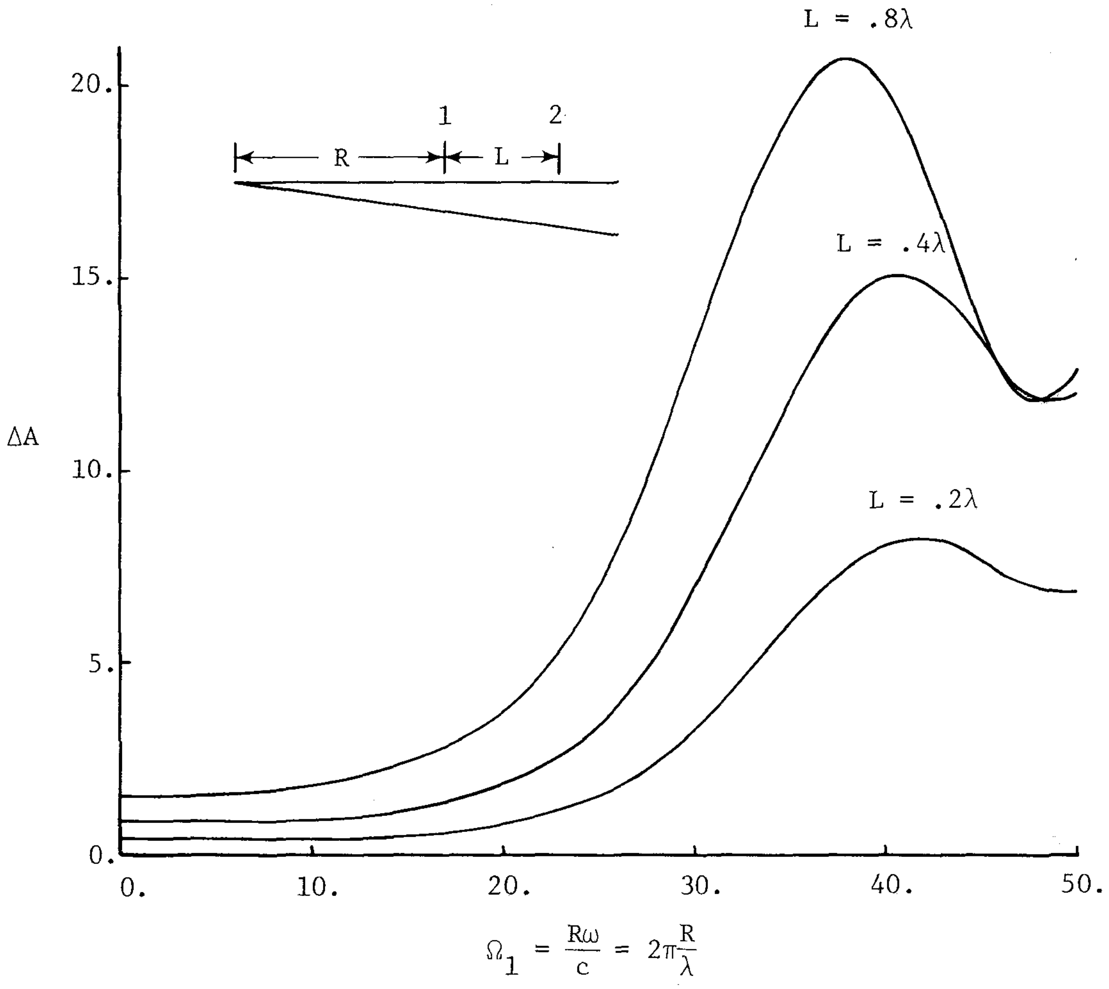

Figure 21. The relative velocity spectrum for various gagelengths ($\gamma = 3°$, $V_o = 3c$).

multiple of π; and minimum, equal to $|A_1-A_2|$, for even multiples. The relative phase, ΔP, is irrelevant.

As an example consider a 3^o wedge. In the range of Ω for maximum amplification, e.g. $\Omega \simeq 40$ in Fig. 12, referring to Fig. 13 the Ω increment, $\Omega_2-\Omega_1$, corresponding to a phase difference of π, is approximately 5. From the definition of Ω

$$\Omega_2-\Omega_1 = \frac{2\pi}{\lambda}(r_2-r_1) = 2\pi\frac{L}{\lambda} ,$$

the gagelength giving maximum relative velocity is found to be $L \simeq .8\lambda$. The relative velocity spectrum for a range of gagelengths is shown in Fig. 21. It is seen that even over distances on the order of 20-30% of a wavelength, relative motion amplification is fairly high. Note that these results are not normalized as were the rotation spectra.

APPROXIMATE SOLUTIONS FOR THE DIPPING LAYER

The previous wedge analysis was based on the assumption that the impedance mismatch between the dipping layer and halfspace was very high. For moderate mismatch the wave system is complicated by strong interaction across the interface, thus allowing energy in the dipping layer to leak into the halfspace. This interaction also includes the presence of supercritically reflected plane waves (Appendix A) and head waves.

Consider the situation depicted in Fig. 22, where the wavespeed in the halfspace is twice that in the dipping layer. As the point of reflection passes the edge of the dipping layer, the entire wave system is instantaneously generated as shown, and expands linearly with time. The transmitted wave reflects off the free surface and then off the interface. Because the point of reflection on the

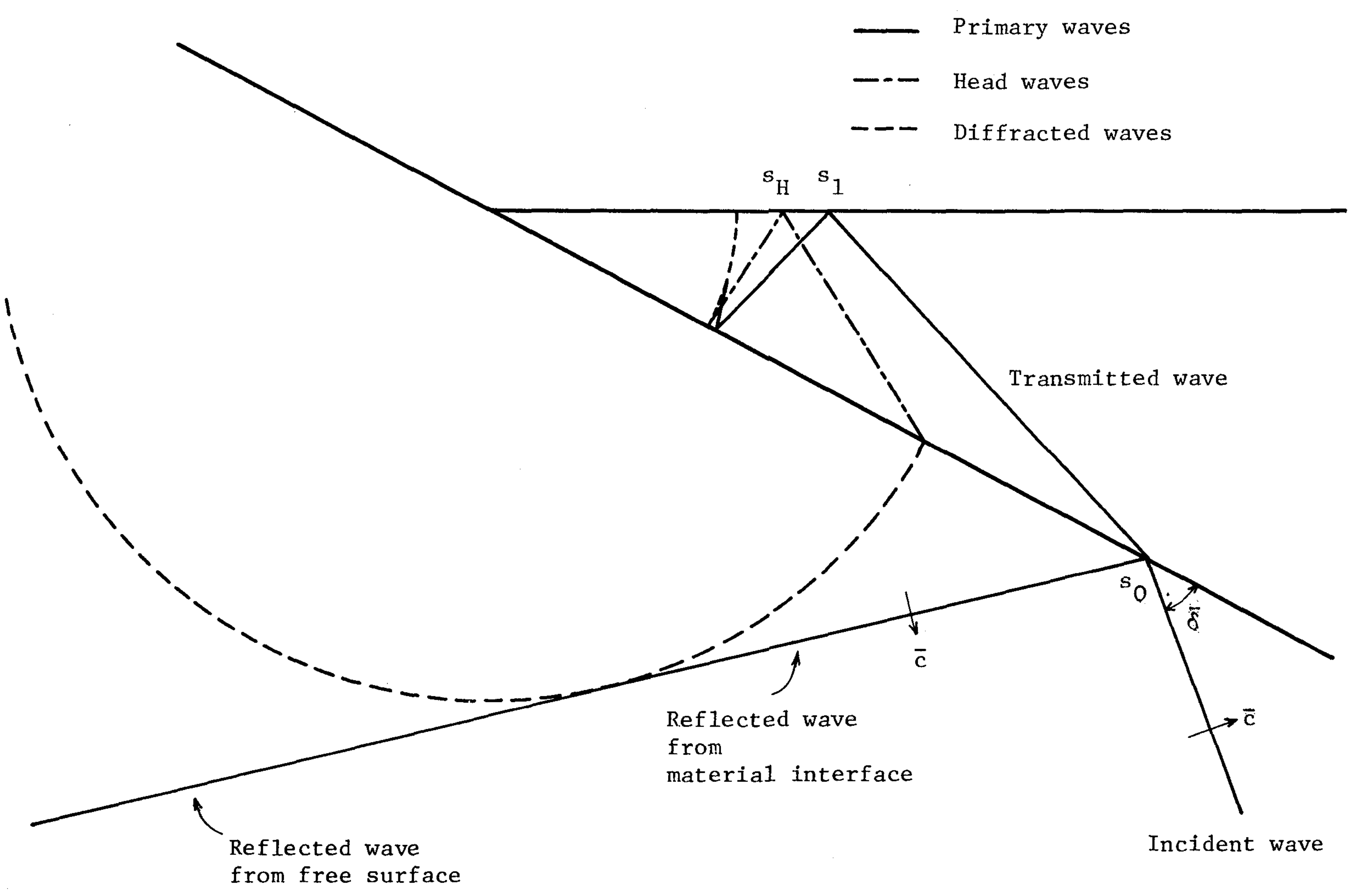

Primary waves
Head waves
Diffracted waves
s_H
s_1
Transmitted wave
s_0
$\bar{\delta}$
$\bar{c}$
$\bar{c}$
Reflected wave from material interface
Incident wave
Reflected wave from free surface

Figure 22. The complete wave system in the dipping layer and halfspace ($\gamma = 28^\circ$, $\bar{c}/c = 2$, $\bar{\delta} = 40^\circ$).

interface is behind the diffracted cylindrical front in the halfspace, no refracted wave exists and the reflection is supercritical (total internal reflection). Note however, that if the point of interface reflection were in front of the diffracted wave, a refracted wave would appear (partial reflection), thus leaking energy from the dipping layer into the halfspace. The waves due to multiple reflection (sub or supercritical) of the transmitted wave in the dipping layer, are called primary waves here.

When a plane step reflects supercritically off an interface, as discussed in Appendix A, the wavefront singularity is converted from a simple step to a step plus a logarithm (singular at the front). This yields a system of head waves in the layer. In addition, as the diffracted cylindrical front in the halfspace grazes the interface, it excites secondary head waves. Note that these secondary waves are intimately connected with the diffracted wave in the halfspace, whereas the primary waves are not.

These observations, in conjunction with the previous wedge analysis, suggest that a useful approximation for moderate impedance mismatch would be to neglect the diffracted waves in the layer and halfspace entirely, in favor of the primary waves. Such solutions should indicate the range of parameters for which anomalous surface behavior can be expected in a realistic dipping formation.

Time Domain Analysis of the Primary Wave System

From results in Appendix A (Case 1) the transmitted step in the dipping layer has amplitude T = 1+R, where R is the interface reflection coefficient of the input wave from the halfspace. In the previous wedge analysis this transmitted wave experienced multiple internal reflections with a sign change only. However, for moderate impedance mismatch the amplitude as well as the nature of the wavefront singularity changes at each reflection. This behavior is derived in Appendix A (Cases 2 and 3). The resulting surface velocity for an incident step can be written as

$$v = \sum_{n=1}^{J} \left[-a_n(1-H(s-s_{2n-1})) + b_n \ln \left| s-s_{2n-1} \right| \right] , \tag{30}$$

where a_n and b_n follow from (A-19, 20, 21). Note that the logarithm in (30) yields a precursor which travels ahead of the point of reflection. This leading disturbance is actually carried on head waves excited on the interface and therefore cannot extend ahead of the leading head wave, which reflects off the surface at $s_H = \frac{c}{\bar{c}}$ (e.g. Fig. 22).

Frequency Domain Analysis of the Primary Wave System

Surface response to harmonic input is calculated in the same manner as before, Eq's. (17)-(25). To obtain the Fourier transform of the acceleration response, (30) is differentiated and substituted into (19), giving

$$\tilde{a}_R^{\delta} = \int_{s_1}^{1} e^{i\Omega s} \sum_{n=1}^{J} \left[a_n \delta(s-s_{2n-1}) + \frac{b_n}{s-s_{2n-1}} \right] ds .$$

The range of integration extends from the leading transmitted wave reflection to the diffracted front at s = 1. Interchanging the order integration and summation and integrating the delta function by inspection gives

$$\tilde{a}_R^{\delta} = \sum_{n=1}^{J} \left[a_n e^{i\Omega s_{2n-1}} + b_n \int_{s_H}^{1} \frac{e^{i\Omega s}}{s-s_{2n-1}} ds \right] ,$$

where the range of integration of the head wave is from $s_H = c/\bar{c}$ to 1. Rewriting the above principal value integral as

$$\int_{s_H}^{1} \frac{e^{i\Omega s}}{s-s_{2n-1}}\, ds = \int_{-\infty}^{\infty} (\ )ds - \int_{-\infty}^{s_H} (\ )ds - \int_{1}^{\infty} (\ )ds \ ,$$

the first integral on the right can be evaluated by residue theory giving

$$\int_{-\infty}^{\infty} \frac{e^{i\Omega s}}{s-s_{2n-1}}\, ds = i\pi e^{i\Omega s_{2n-1}} \ ,$$

while the second and third integrals can be shown, by the method of stationary phase, to decay like $1/\Omega$. Because the resonance peaks are expected to appear in the high frequency range, these latter integrals can be safely neglected. Therefore the Fourier transform of the acceleration response due to primary waves is

$$\tilde{a}_R^{\delta}\Big|_{\text{primary waves}} = \sum_{n=1}^{\infty} (a_n + i\pi b_n)\, e^{i\Omega s_{2n-1}} + O(1/\Omega) \ . \qquad (31)$$

Calculating the amplitude and phase spectra as before, the harmonic velocity response is

$$v = A(\Omega) \sin(\omega t - P(\Omega)) \ .$$

A velocity amplitude spectrum is shown in Fig. 23 for a 3° and 6° dipping layer. The incidence angles, $\bar{\delta}$, were chosen to nearly maximize response for the assumed material properties, i.e. all interface reflections were supercritical. Comparison with results for the wedge, Fig. 12, shows essentially the same spectral behavior. Note that the normalization used here is, as before, $v_o = 2\bar{v}_o$, hence the above amplitude spectra give amplification relative to motion on the halfspace, to the left of the dipping layer, Fig. 7.

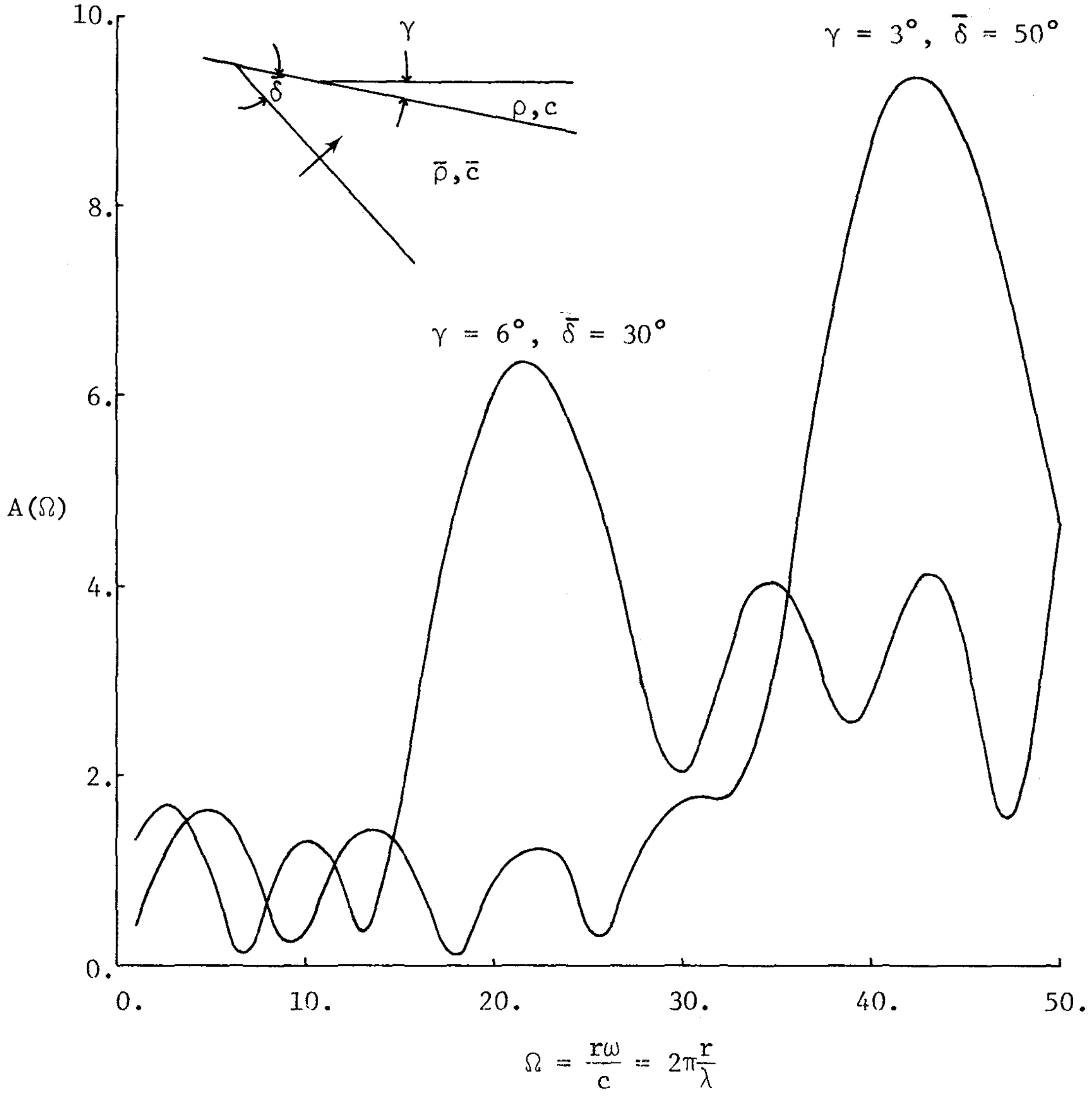

Figure 23. Approximate velocity amplitude spectra for moderate dip angles, with $\bar{c}/c = 3$, $\bar{\rho}/\rho = 1.27$.

In the wedge analysis the variation of amplification with incidence angle (more precisely, with $V_o = \bar{c}/\sin\bar{\delta}$) was quite smooth, Fig. 14. However, for the dipping layer the dependence on incidence angle is highly discontinuous as illustrated in Fig. 24. The mechanism is transition from subcritical to supercritical interface reflection. For example, referring to the case in Fig. 24, at normal incidence the initial transmission coefficient, T, is 1.65 but the transmitted wave reflects subcritically twice off the interface, thus the first primary wave to be supercritically reflected, i.e. trapped, has a coefficient of .53. This situation persists with a decrease in transmission coefficient until the incidence angle reaches something over 10^o at which point the second subcritical reflection becomes supercritical. At a little over 36^o the remaining subcritical reflection transitions, thus all of the transmitted energy is trapped by the dipping layer for incidence angles beyond approximately 38^o. A similar process occurs for other dip angles and material properties, however, with shallow dip angles, on the order of 1^o or so, the dependence on incidence angle is quite extreme for near-grazing incidence. Such a case is illustrated in Fig. 25 for a dip of 1^o. For near-normal incidence there are 45 free surface reflections, 9 of which are due to subcritical interface reflection. The amplification of 3.6 at $\bar{\delta} = 0$ occurs for $\Omega = 90$, in agreement with simple one-dimensional theory for a uniform layer over a halfspace. As the incidence angle increases, the subcritical reflections gradually transition while the transmission coefficient decreases, causing a net decrease in amplification. The trend of 1-D theory is indicated by the dashed curve. The first peak noticeable in Fig. 25 corresponds to a transition from 4 to 3 subcritical reflections, the second from 3 to 2, the third from 2 to 1, and the pronounced final peak from 1 to 0. This last peak, with an amplification of 17, occurs at $\Omega = 125$, corresponding to approxi-

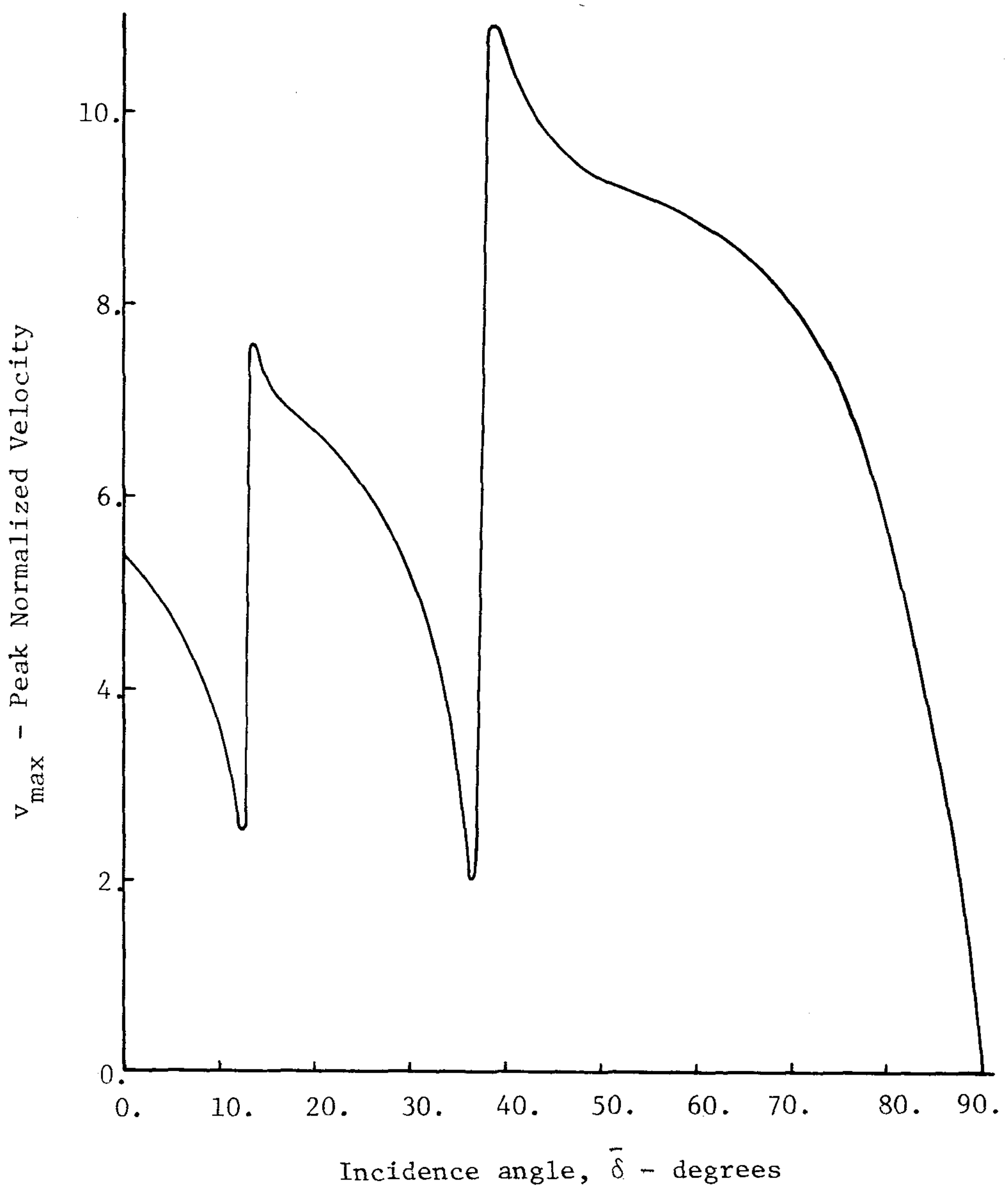

Figure 24. Variation of peak normalized velocity, with incidence angle, for $\gamma = 3°$, $\bar{c}/c = 3.75$, $\bar{\rho}/\rho = 1.27$.

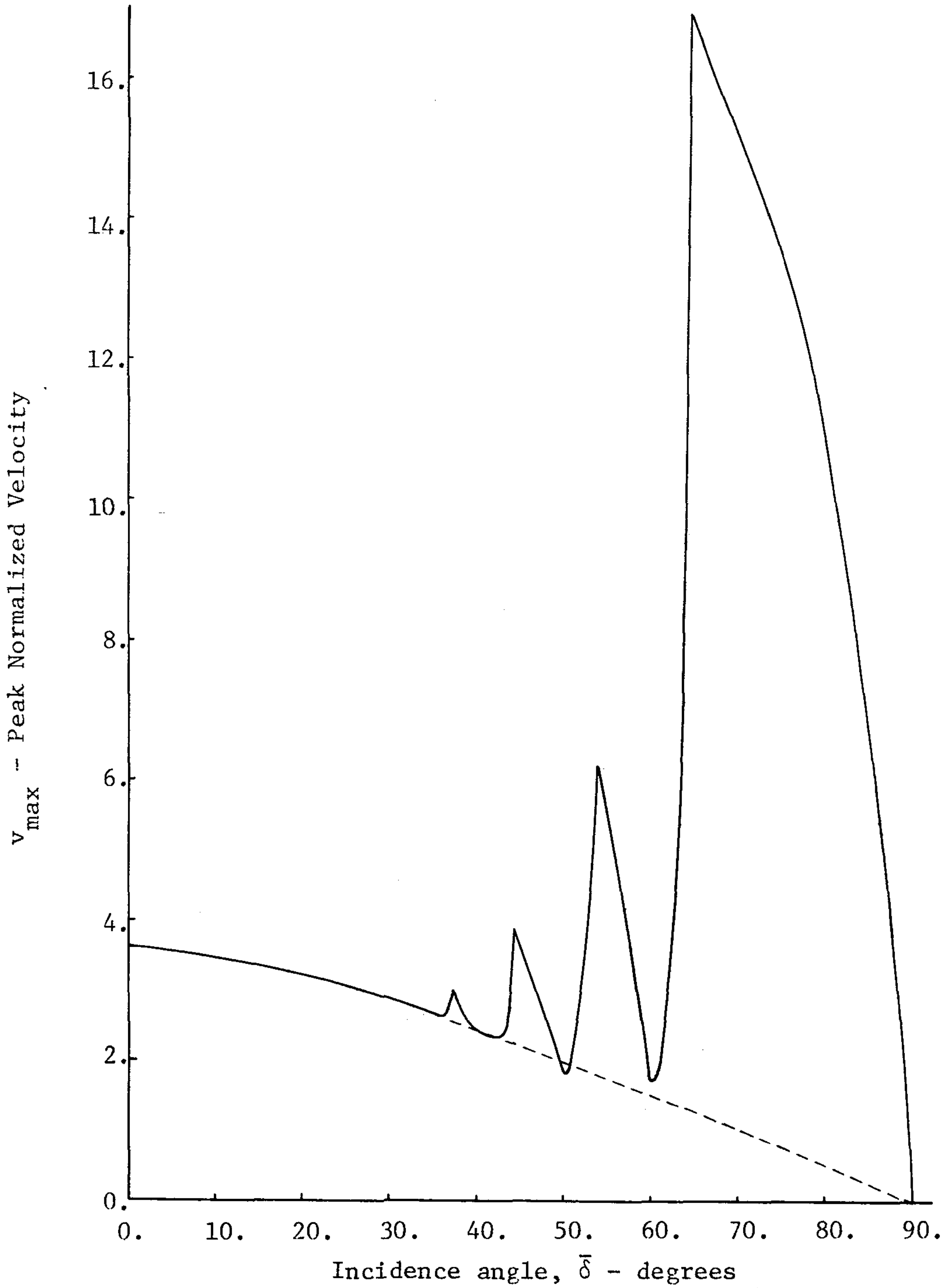

Figure 25. Variation of peak normalized velocity with incidence angle, for $\gamma = 1°$, $\bar{c}/c = 3$, $\bar{\rho}/\rho = 1.27$. The dashed curve shows the trend of 1-D theory.

mately 20 wavelengths from the edge of the dipping layer for a fixed frequency input; the interference pattern on the surface is due to 36 sine waves, each with normalized amplitude of 1.26.

The dependence of maximum amplification on the wavespeed ratio is indicated in Fig. 26. The wavespeed ratios are meant to correspond approximately (in increasing order) to young bay sediments, alluvial deposits, and older sedimentary deposits over bedrock. The data points correspond to maxima found by sampling at 10° increments in incidence angle, hence the scatter. Nonetheless, these results show that even for moderate ratios on the order of 2, amplifications of 6 to 7 can be expected. The curves seem to indicate an overall difference between small dip behavior, for angles $\leq 4^\circ$, and large dip behavior, $\geq 6^\circ$.

In the wedge analysis it was shown that surface rotational and relative motion amplification spectra were maximized near the peaks of the velocity amplitude spectra. The same results are found here for the primary wave system, e.g. amplifications of 20 or more over the rotational and relative motion encountered on the halfspace to the left of the dipping layer, Fig. 7. Plots corresponding to Figs. 18 and 21 will not be reproduced.

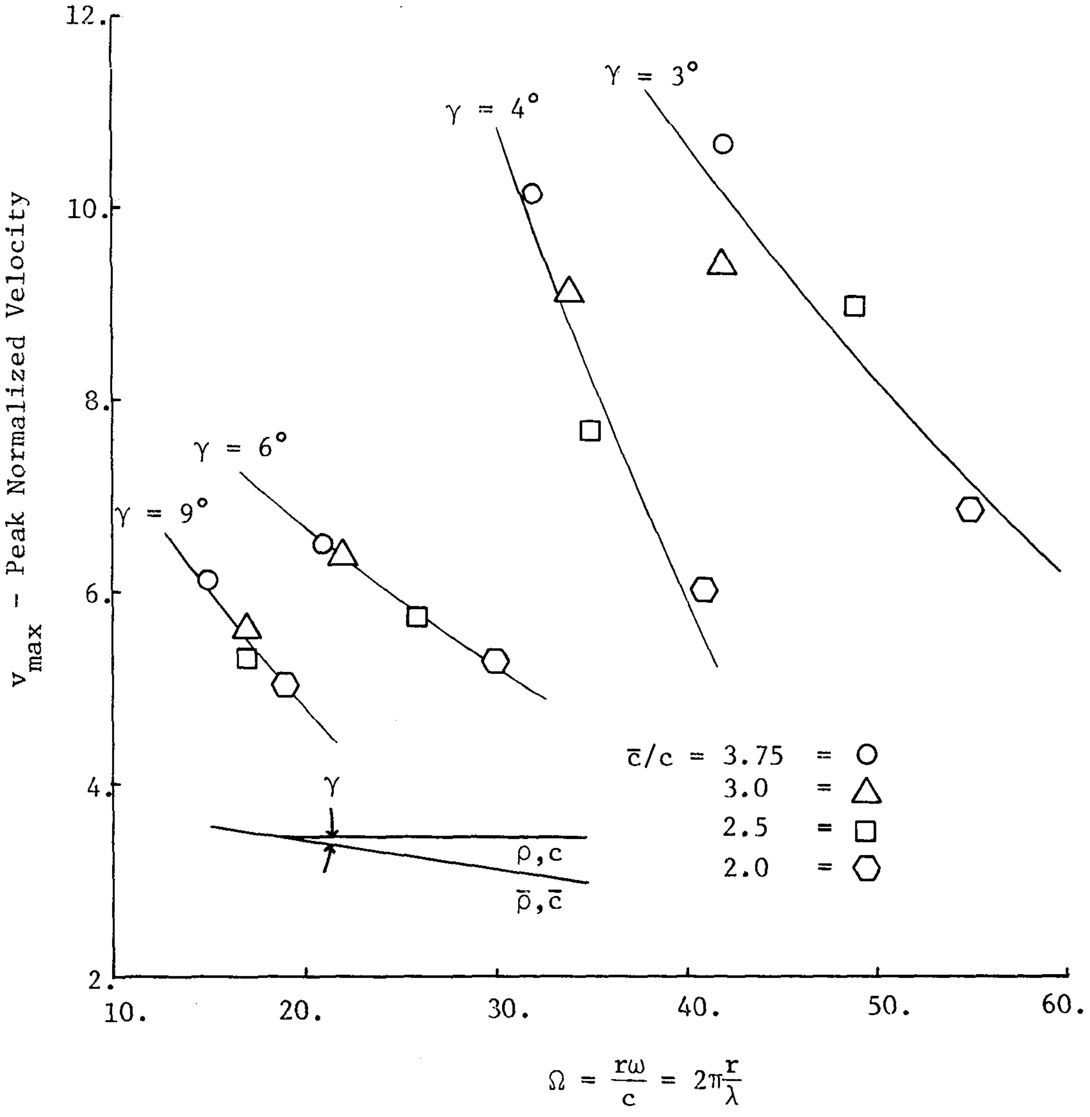

Figure 26. Variation of peak normalized velocity with wavespeed ratio, $\bar{c}/c$, for a range of dip angles, γ, with $\bar{\rho}/\rho = 1.27$.

REFERENCES - PART II

Achenbach, J. D. (1970). Shear waves in an elastic wedge, Int. J. Solids Structures 6, 379-388.

Copson, E. T. (1967). Asymptotic Expansions, Cambridge University Press.

Keller, J. B. and A. Blank (1951). Diffraction and reflection of pulses by wedges and corners, Communs. on Pure and Appl. Math. 4, 75-94.

Wojcik, G. L. (1977). Self-similar elastodynamic solutions for the plane wedge, Ph.D. thesis, Caltech.

CONCLUSION

Summary

Results of the literature survey in Part I indicate that our understanding of effects due to laterally inhomogeneous geologic structures on free field response to earthquakes is qualitative and incomplete. Common structures like dipping transition layers and alluvial basins have been identified and investigated by means of analytical, numerical and model studies. Unfortunately the complexity of the problems in terms of geometry and input have precluded a good understanding of the mechanisms and phenomena involved. It was noted in this context that the simplest realistic geometry and input for a laterally inhomogeneous halfspace model was the surface dipping layer with plane SH waves incident from below, because it lacked a characteristic length. No published analyses of this case were found and it was concluded that such should be performed, thus motivating Part II. A complete discussion and conclusions of the survey are included at the end of Part I.

In Part II, analysis of the dipping layer with plane SH inputs was performed in two stages. First, the layer and underlying halfspace were decoupled by assuming a high density mismatch between the two, thus allowing the layer to be idealized as a wedge with upper face stress free and prescribed velocity on the lower face. In this way the general nature of the diffracted and plane wave system in the layer was determined without the complication of wave coupling across the interface. Second, on the basis of the wedge solution it was shown that diffraction effects were negligible, whence the coupled dipping layer and halfspace were analyzed for a range of velocity ratios by including primary (non-diffracted) wave contributions only. For both the wedge and dipping layer, surface response was first evaluated in the time domain for a plane step in SH particle velocity propagating in the downdip direction at arbitrary incidence angles. From this, frequency domain response was found by convolution.

Results of the time domain wedge analysis showed that on the surface, the incident step was converted to a series of pulses propagating outward from the edge. This surface response was due to multiple reflections of plane waves between the wedge faces, with the incidence angle increasing by the wedge angle at each reflection. The number of surface pulses depended primarily on the wedge angle and to a lesser extent on the incidence angle (increasing as the angles decreased). The leading pulse had the highest phase velocity, which decreased for subsequent pulses, approaching the velocity of shear waves in the layer, c. A single diffracted wave, traveling outward at c, provided a transition between the plane wave solution, i.e. the pulses, and the long time solution at the edge, where the velocity was constant.

The frequency domain wedge analysis yielded two constant amplitude sinusoidal wavetrains traveling outward from the edge for each time domain pulse, i.e. one (primary) wavetrain for each free surface reflection of the trapped plane wave. The phase velocity was different for each wavetrain, decreasing from some maximum and approaching c. The diffracted wave contributed a single (secondary) wavetrain with phase velocity, c, and amplitude decaying like $1/\sqrt{r\omega}$. The major feature of the frequency domain response was the interference pattern on the surface due to constructive and destructive interference of the outgoing waves. This was expressed as a function of the nondimensionalized frequency, $\Omega \equiv \frac{r\omega}{c} = 2\pi\frac{r}{\lambda}$, interpreted here as a spatial coordinate (scaled distance from the edge) for fixed frequency input. For low frequency, i.e. low Ω, close to the edge, interference was primarily destructive, with the response dominated by the diffracted wave.

However, for higher frequency, further from the edge, constructive interference of the numerous nondecaying primary waves produced standing waves and zones of resonance , where translational motion was on the order of 6-15 times the lower face input motion. The amplifications were highest for small wedge angles, e.g. $\leq 4^{\circ}$, with shallow input incidence, because such cases maximized the number of free surface reflections, hence the number of primary wavetrains. It was also found that the resonance zones produced amplifications of rotational motion on the order of 20-50 times the corresponding input, and amplified relative motion on the order of 10-20 times. For the smaller wedge angles the resonance zones typically started at values of Ω greater than 35, corresponding to distances from the edge of approximately 5 wavelengths.

The original problem of the dipping layer over a halfspace was analyzed approximately by neglecting all secondary (diffracted) wave contributions. This approximation was based on the observation that resonance zones on the wedge surface occurred in the higher frequency range, where diffraction effects were negligible due to the $1/\sqrt{\Omega}$ decay. In contrast to the wedge analysis, the primary wave system in the layer was complicated by multiple subcritical (partial) and supercritical (total) reflections at the interface, and head waves. The time domain analysis showed that the series of pulses found for the wedge was modified by changes in pulse amplitude and logarithmic singularities due to multiple partial and total interface reflections, respectively. The total reflections produced head wave precursors.

Frequency domain analysis of the dipping layer showed essentially the same resonance zone behavior as for the wedge, with high amplication of translational, rotational and relative surface motion. The principal difference was for shallow incidence angles, where the first few internal reflections were generally subcritical and leaked much of the incident energy back into the halfspace. As the incidence angle increased, the number of subcritical reflections decreased until at a certain angle all of the incident energy was trapped. This effect was particularly dramatic for small dip angles, e.g. 1^{o}, where for incidence beyond about 65^{o} the resonance zone produced translational motion on the order of 17 times that predicted by modeling the 1^{o} dipping layer as a uniform layer over a halfspace.

Discussion

The most striking feature of the surface effects due to a dipping layer is the marked enhancement of ground motion in either the time or frequency domain. The physical mechanism for this phenomenon is the down dipping interface (with respect to the incident wave) which tends to increase the internal incidence angle of the initial transmitted wave so that it becomes trapped by total reflection at the interface. The trapped wave then undergoes multiple reflections between the free surface and interface with the incidence angle increasing by the dip angle at each reflection. Each free surface reflection contributes to the surface motion. In the time domain this mechanism converts an incident pulse into a series of surface pulses; while in the frequency domain an incident harmonic wave is converted to a series of harmonic waves which interfere constructively on the surface yielding a system of standing waves and so-called resonance zones. Note that such a mechanism is applicable to P and SV wave propagation, as well as to the SH case considered here.

The time domain solution is best appreciated in the context of structural response. Recall that the frequency parameter, $\Omega = \frac{r\omega}{c}$, can be viewed as a spatial or frequency coordinate. For harmonic input with ω fixed, it was natural to take Ω as a scaled spatial coordinate; however, for transient input it is appropriate to consider r fixed and associate ω with the natural frequency of structural response. Assume that the structure, modeled as an undamped single degree of freedom oscillator, is coupled to a component of surface motion (either translational, rotational or relative), e.g. the translational component, w. Then the equation governing $y = x - w$, the relative displacement, is

$$m\ddot{y} + ky = -m\ddot{w} \quad , \tag{32}$$

where $\ddot{w}$ is the transient surface acceleration input. Of interest here is the amount of energy imparted to the structure by the surface motion, hence only the long time response need be calculated. Solving (32) by means of, for example, Laplace transforms or the Duhamel superposition formula, (16), yields for large t

$$\begin{aligned} \dot{y} &= \mathrm{Re}-e^{-i\omega t} \int_0^\infty e^{i\omega t}\, \ddot{w}dt \\ &= A(\Omega)\ \sin(\omega t - P(\Omega) - \pi/2) \quad , \end{aligned} \tag{33}$$

where $\omega = \sqrt{\frac{k}{m}}$ is the natural frequency of the oscillator, and A and P are the amplitude and phase of the Fourier transform of the transient acceleration history. Therefore the oscillator response spectrum and the dipping layer amplitude spectrum are the same, $A(\Omega)$; and it follows that resonance zones appear in the time as well as the frequency domain. For example, at a given distance, r, from the edge, the structures (characterized by ω) most prone to shaking and damage are those for which $A(\frac{r\omega}{c})$ is maximized. Conversely, given a structure with natural frequency, ω, then it is most vulnerable at the distance which maximizes $A(\Omega)$. In either case the motion can be amplified by as much as an order of magnitude, if not more.

Regarding the applicability of solutions derived here to modeling real seismic inputs, note that the dipping layer can be excited in the near or far seismic source field. For near-field excitation the time domain solution, for a plane SH step incident at arbitrary angle from below, appears to be a valid model (after convolution with the source time function). For far-field excitation, however, both the time and frequency domain solutions are of questionable validity because surface waves, i.e. Love waves, typically dominate the input, rather than body waves. Recalling that Love waves are due to total reflection and constructive interference of plane waves in near surface layers, e.g. Fig. 27, it appears that plane wave solutions of the type derived here are in fact applicable and could be used to model Love wave inputs. For example, in the case of harmonic Love waves propagating toward the layer as in Fig. 27, an approximate solution could be constructed by resolving the Love wave into its predominate multiply reflected harmonic wavetrains, computing the layer response to each and superposing the results.

One final observation is that in the frequency domain, any resonance zone, with a peak at Ω_o say, occurs at a fixed distance from the edge for constant input frequency. Consequently when the frequency changes, the resonance zone shifts its location so that Ω_o remains fixed. In particular, if a maximum in the standing wave pattern is located at r, and $\Delta\omega$ is the frequency change, then

$$\Omega_o = \frac{r\omega}{c} = \frac{(r + \Delta r)(\omega + \Delta\omega)}{c} ,$$

from which

$$\lim_{\Delta\omega \to 0} \frac{\Delta r}{\Delta\omega} = \frac{dr}{d\omega} = \frac{-r}{\omega} ,$$

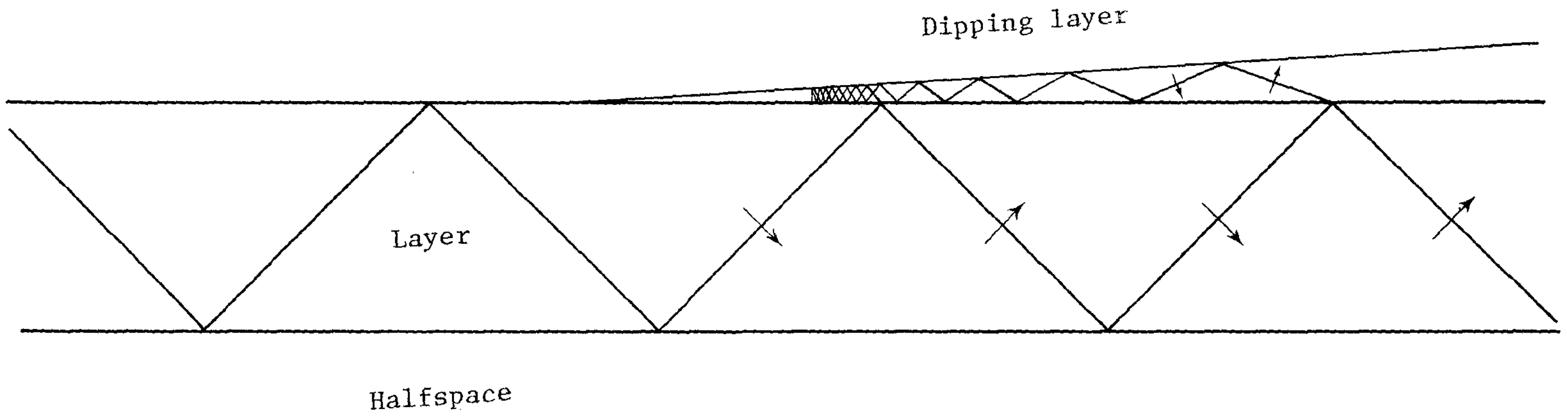
Dipping layer
Layer
Halfspace

Figure 27. A schematic of Love wave propagation in a surface layer overlain by a dipping layer.

hence the speed at which the maximum travels is

$$\dot{r} = \frac{-r}{\omega}\dot{\omega} = \frac{-c\Omega_o}{\omega^2}\dot{\omega} . \qquad (34)$$

Assuming a 1 Hz input, for example, a maximum at $\Omega_o = 40$ would travel at $\dot{r} \simeq -c\dot{\omega}$. Presumably $\dot{\omega}$ would be something less than unity so the speed of the traveling resonance zone would be a fraction of the wavespeed in the layer. This argument applies to a single harmonic input, and similarly for a superposition of harmonic inputs at different incidence angles and frequencies, e.g. from the above Love wave approximation. In the case of a dispersed Love wave transient, $\dot{\omega}$ would be obtained from the dispersion relation. As noted by Trifunac (1971), the presence of standing wave patterns could explain numerous observations of visible waves during earthquakes, Richter (1958). Resonance zones over a dipping layer, traveling by virtue of changing input frequency, is a possible mechanism for such visible wave phenomena.

Conclusions

Some obvious applications of the results found in this report are to local seismic zonation, critical facility siting, building rehabilitation and soil failure. In seismic zonation studies, sedimentary and alluvial deposits over baserock are usually modeled as horizontal layers, to first order, whereas in many cases the layering is inclined. The existence of resonance zones and high amplifications over an inclined interface suggests that in certain situations the layer inclination must be included in assessing seismic response. Similarly, in critical facility siting, sites are typically modeled as stacks of horizontal layers with shear waves incident normally from below. If the site has inclined interfaces and waves are not vertically propagating, then as results for the dipping layer show, this simple model can be grossly conservative. In terms of building rehabilitation to withstand the effects of earthquakes, clearly all substandard structures cannot be reinforced; however, on the basis of subsurface geology, e.g. dipping layers, sites could be ranked, and particularly vulnerable structures identified. Regarding soil failure, resonance zones are certainly relevant to the liquifaction and landslide potential of inclined soil deposits over baserock.

Anomalous surface behavior due to a dipping layer has been obtained for the case of downdip propagation of incident plane waves. Intuitively, it might be expected that updip propagation and the resulting "beach" effect would yield stronger motion; however, updip incidence is actually deamplifying except when the impedance mismatch is very high. Although such results are not shown, the beach effect occurs only with an extreme mismatch, yielding results similar to and with some enhancement over downdip propagation.

An interesting speculation regarding Love waves is that lateral inhomogeneities, particularly down-dipping formations with suitably incident body waves, tend to promote the conversion of body waves to trapped surface waves, which presumably exhibit themselves as Love waves. This and other observations concerning Love waves need further investigation. An analytical basis would be the superposition of multiply reflected plane waves in a layer overlain by a dipping layer, illustrated in Fig. 27 and described in the above discussion.

In conclusion, it appears that dipping layers and similar inclined formations can have pronounced effects on surface motion during earthquakes. This is based on results of a linear analysis, modeling the geologic formations as elastic continuua. In order to confirm the applicability of these results to real situations, correlation of actual damage or shaking during earthquakes with subsurface conditions must be made. In addition, numerical model studies with nonideal geometries and realistic nonlinear material properties should be performed to determine their effect.

REFERENCES - CONCLUSION

Richter, C. F. (1958). Elementary Seismology, W. H. Freeman and Co., San Francisco.

Trifunac, M. D. (1971). Surface motion of a semi-cylindrical alluvial valley for incident plane SH waves, Bull. Seism. Soc. Am. 61, 1755-1770.

APPENDIX A

REFLECTION AND REFRACTION OF PLANE SH WAVES

Consider reflection and refraction of a plane SH wave incident on a plane interface as shown in Fig. A-1. In the upper halfspace the mass density, shear modulus and wavespeed are ρ, μ, $c = \sqrt{\frac{\mu}{\rho}}$, respectively, and v is the particle velocity. Corresponding quantities in the lower halfspace are barred, e.g., $\bar{v}$. Under the transformation, $p = x-Vt$, to a system of coordinates moving with the point of reflection at $V = c/\sin\delta$, the governing 2-D wave equations on particle velocity become

$$(1-\frac{V^2}{c^2})\, v_{pp} + v_{yy} = 0, \qquad \text{(A-1)}$$

$$(1-\frac{V^2}{\bar{c}^2})\, \bar{v}_{pp} + \bar{v}_{yy} = 0. \qquad \text{(A-2)}$$

These are of mixed type (hyperbolic-elliptic) depending on the ratios, V/c and $V/\bar{c}$. Compatibility and equilibrium across the material interface require that particle velocity and the time derivative of shear stress be continuous, hence at

$$y = 0: \; v = \bar{v}, \qquad \text{(A-3)}$$

$$\mu v_y = \bar{\mu}\bar{v}_y. \qquad \text{(A-4)}$$

Solutions of the governing equations are readily found. In the upper halfspace $V/c = 1/\sin\delta$ is always greater than unity, hence (A-1) reduces to the one-dimensional wave equation with solution,

$$v(p,y) = G_+(p+\alpha y) + G_-(p-\alpha y), \qquad \text{(A-5)}$$

$$\alpha \equiv \sqrt{(V/c)^2-1} = \cot\delta,$$

where $p \pm \alpha y$ are characteristic coordinates and $G_\pm$ are distinct functions. In the lower halfspace, when $V/\bar{c} > 1$ (subcritical reflection), (A-2) also reduces to the wave equation with

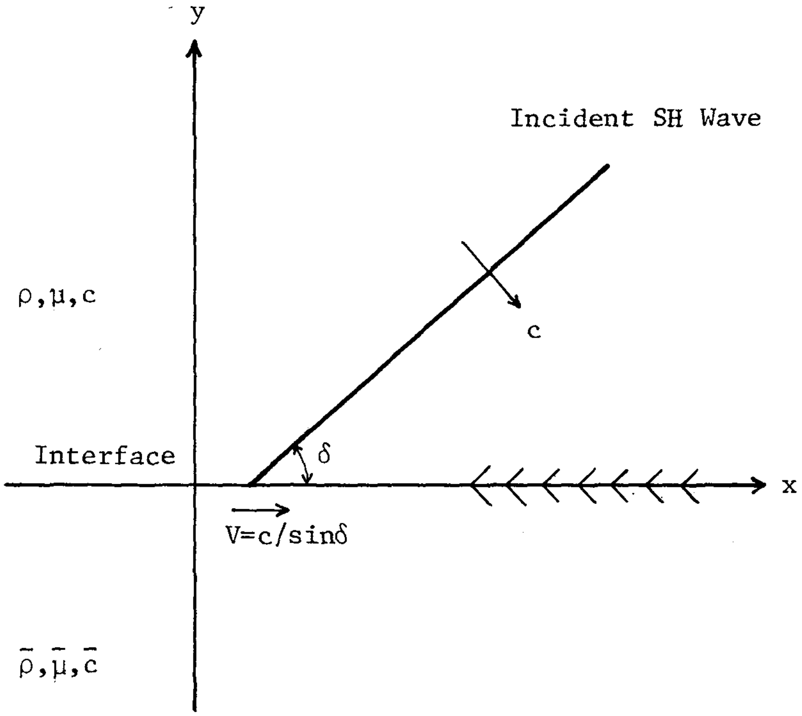
y
Incident SH Wave
ρ,μ,c
c
Interface
δ
x
V=c/sinδ
$\bar{\rho},\bar{\mu},\bar{c}$

Figure A-1. Plane SH wave incident on a material interface (y=0).

$$\bar{v}(p,y) = \bar{G}_+(p+\bar{\alpha}y) + \bar{G}_-(p-\bar{\alpha}y), \qquad \text{(A-6)}$$

$$\bar{\alpha} \equiv \sqrt{(V/\bar{c})^2-1} = \cot\bar{\delta},$$

where $\bar{\delta}$ is the acute angle between the characteristic and the p axis (i.e., the angle of refraction). However, when $V/\bar{c} < 1$ (supercritical reflection), (A-2) reduces to Laplace's equation with solution,

$$\bar{v}(p,y) = \mathrm{Re}\bar{G}(p+i\bar{\beta}y) \equiv \bar{g}(p,\bar{\beta}y), \qquad \text{(A-7)}$$

$$\bar{\beta} \equiv \sqrt{1-(V/\bar{c})^2},$$

where $\bar{G}$ is an analytic function of the complex variable, $p+i\bar{\beta}y$, and Re designates the real part.

In the following, transmission and/or reflection coefficients of use in this report are obtained for the cases of subcritical and supercritical reflection.

Case 1: Subcritical reflection of a plane step

In this case $V/\bar{c} = \dfrac{c/\bar{c}}{\sin\delta} > 1$ and the characteristics are depicted in Fig. A-2. An incident unit step in SH particle velocity is assumed on the $p-\alpha y=0$ characteristic as

$$G_-(p-\alpha y) = 1-H(p-\alpha y). \qquad \text{(A-8)}$$

Because $\bar{c} < V$ no disturbance can travel ahead of the point of reflection (on the $p+\bar{\alpha}y$ characteristic) hence $\bar{G}_+ \equiv 0$ and the remaining unknowns are G_+ and $\bar{G}_-$. Substituting the hyperbolic solutions, (A-5,6), into the interface conditions, (A-3,4), gives

$$G_+(p) + 1 - H(p) = \bar{G}_-(p),$$

$$\mu\left[\alpha G_+'(p) + \alpha\delta(p)\right] = \bar{\mu}\left[-\bar{\alpha}\bar{G}_-'(p)\right].$$

Solving for the unknowns and integrating yields

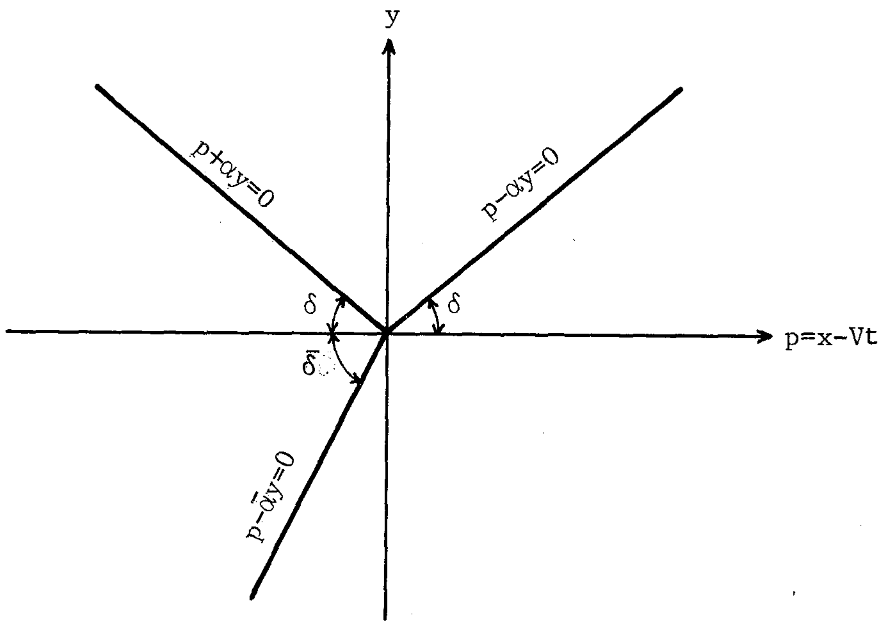

y
p+αy=0
p-αy=0
δ
δ
$\bar{\delta}$
p=x-Vt
p-$\bar{\alpha}$y=0

Figure A-2. Characteristics for the case of subcritical reflection.

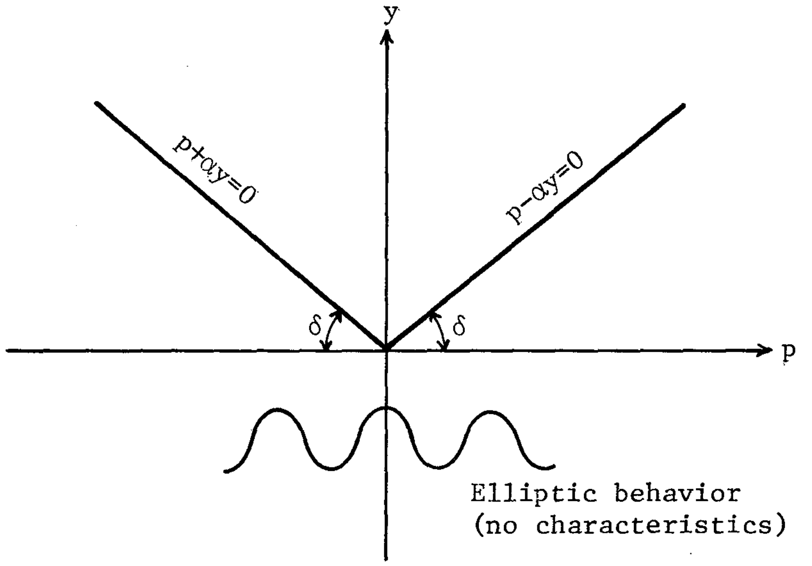

y
p+αy=0
p-αy=0
δ
δ
p
Elliptic behavior
(no characteristics)

Figure A-3. Characteristics for the case of supercritical reflection.

$$G_+(p+\alpha y) = R\left[1-H(p+\alpha y)\right], \qquad \text{(A-9)}$$

$$\bar{G}_-(p-\bar{\alpha}y) = T\left[1-H(p-\bar{\alpha}y)\right], \qquad \text{(A-10)}$$

with the reflection and transmission coefficients expressed as

$$R = \frac{\mu\alpha-\bar{\mu}\bar{\alpha}}{\mu\alpha+\bar{\mu}\bar{\alpha}} = \frac{\cos\delta-I^2\cos\bar{\delta}}{\cos\delta+I^2\cos\bar{\delta}}, \qquad \text{(A-11)}$$

$$T = R + 1, \qquad \text{(A-12)}$$

where $\bar{\delta}$ follows from Snell's law,

$$\frac{\sin\bar{\delta}}{\sin\delta} = \frac{\bar{c}}{c},$$

and I is the impedance ratio,

$$I \equiv \sqrt{\frac{\bar{\rho}\bar{c}}{\rho c}}.$$

Case 2: Supercritical reflection of a plane step

Here $V/\bar{c} = \dfrac{c/\bar{c}}{\sin\delta} < 1$ and no characteristics exist in the lower halfspace, Fig. A-3. Again the incident wave is taken as (A-8). Substituting (A-5,7) into the interface conditions gives

$$G_+(p) + 1 - H(p) = \bar{g}(p), \qquad \text{(A-13)}$$

$$\mu\left[\alpha\, G_+'(p) + \alpha\delta(p)\right] = \bar{\mu}\bar{g}_y(p), \qquad \text{(A-14)}$$

and eliminating $G_+(p)$ by differentiation yields

$$\mu\alpha\, \mathrm{Re}\bar{G}'(p) + \bar{\mu}\beta\, \mathrm{Im}\bar{G}'(p) = -2\mu\alpha\delta(p). \qquad \text{(A-15)}$$

The definition for the derivation of an analytic function,

$$\bar{G}'(p+i\beta y) = \bar{g}_p(p,y) - i\,\frac{1}{\beta}\bar{g}_y(p,y),$$

was used to obtain this form. The above expression implies that the analytic function, $\bar{G}$, has a simple pole at the origin. Assuming the form,

$$\bar{G}'(p+i\beta y) = \frac{a+ib}{p+i\beta y}, \qquad \text{(A-16)}$$

from which

$$\lim_{y\to 0^-} \bar{G}'(p+i\beta y) = (a+ib)\ (\frac{1}{p}+i\pi\delta(p))\ ,$$

and substituting the real and imaginary parts into (A-15) yields the residue,

$$a = \frac{-\frac{2}{\pi}\mu\alpha\bar{\mu}\bar{\beta}}{(\mu\alpha)^2+(\bar{\mu}\beta)^2},\ b = \frac{\frac{2}{\pi}(\mu\alpha)^2}{(\mu\alpha)^2+(\bar{\mu}\beta)^2}\ . \qquad \text{A-17)}$$

To solve for the reflected wave, $G_+(p+\alpha y)$, which is of interest here, (A-16) is integrated (yielding $(a+ib)\mathrm{Log}(p+i\beta y)$) and the real part of its limit as $y\to 0^-$ substituted into (A-13), giving

$$G_+(p) = a\ln|p| + (\pi b-1)(1-H(p)),$$

whence

$$G_+(p+\alpha y) = a\ln|p+\alpha y| + (\pi b-1)\left[1-H(p+\alpha y)\right]. \qquad \text{(A-18)}$$

This result exhibits the well-known property of supercritical reflection, namely, enhancement of the singularity at the wavefront. Note also that because behavior in the lower halfspace is elliptic rather than hyperbolic no energy is propagated away in waves but instead is stored as recoverable elastic strain energy.

Case 3: Supercritical reflection of a supercritically-reflected plane step

Of particular utility in this report is the behavior of a supercritically-reflected plane step as it reflects off a free surface and is again reflected supercritically off an interface. To this end the incident wave is taken as

$$G_-(p-\alpha y) = c\ln|p-\alpha y| + d\left[1-H(p-\alpha y)\right]. \qquad \text{(A-19)}$$

As in the previous case, substituting wave solutions into the interface condit

yields

$$G_+(p) + c\ln|p| + d\left[1-H(p)\right] = \tilde{g}(p),$$

$$\mu\left[\alpha G_+'(p) - \frac{c\alpha}{p} + d\alpha\delta(p)\right] = \bar{\mu}\bar{g}_y(p),$$

from which

$$\mu\alpha \mathrm{Re}\bar{G}'(p) + \bar{\mu}\bar{\beta}\mathrm{Im}\bar{G}'(p) = 2\mu\alpha\left[\frac{c}{p} - d\delta(p)\right].$$

Assuming

$$\bar{G}'(p+i\beta y) = \frac{e+if}{p+i\beta y},$$

and solving for the residue,

$$e = \frac{\frac{2}{\pi}\mu\alpha\left[\pi\mu\alpha c - \bar{\mu}\bar{\beta}d\right]}{(\mu\alpha)^2 + (\bar{\mu}\bar{\beta})^2}, \quad f = \frac{\frac{2}{\pi}\mu\alpha\left[\pi\bar{\mu}\bar{\beta}c + \mu\alpha d\right]}{(\mu\alpha)^2 + (\bar{\mu}\bar{\beta})^2} \quad . \tag{A-20}$$

Finally solving for the reflected wave gives

$$G_+(p+\alpha y) = (e-c)\ln|p+\alpha y| + (\pi f - d)\left[1 - H(p+\alpha y)\right] . \tag{A-21}$$

APPENDIX B

SELF-SIMILAR WEDGE SOLUTIONS IN THE HYPERBOLIC DOMAIN

In the hyperbolic domain (i.e., for $s \equiv \frac{ct}{r} < 1$) a general solution of the equation governing particle velocity has been found as

$$v = V_+(\alpha_+) + V_-(\alpha_-), \qquad \text{(B-1)}$$
$$\alpha_\pm \equiv \theta \pm \cos^{-1}s,$$

where the $\alpha_\pm$ characteristics are straight lines tangent to the unit circle, $s = 1$. An α_+ and α_- characteristic, related by $\alpha_+ + \alpha_- = 2\theta$, passes through each point of the domain. On the free surface boundary, conditions on the solution are

$$\theta = 0: \quad v_\theta = 0 = V_+'(\cos^{-1}s) + V_-'(\cos^{-1}s), \qquad \text{(B-2)}$$

while on the interface between the dipping layer and halfspace, conditions are

$$\theta = \gamma: \; v = V_+(\gamma+\cos^{-1}s) + V_-(\gamma-\cos^{-1}s) = H(s-\frac{c}{V_o}). \qquad \text{(B-3)}$$

The resulting system of wavefronts is readily constructed from knowledge of the characteristics. Fig. B-1 illustrates the wave system for a wedge angle of $\gamma = 28^o$ with $V_o = 3c$.

On the $\theta = \gamma$ face, in a neighborhood of the applied jump in particle velocity (at $s = \frac{c}{V_o} \equiv s_0$ in Fig. B-1), from (B-3)

$$V_-(\gamma-\cos^{-1}s) = H(s-c/V_o),$$

where $V_+(\alpha_+)$ is zero by virtue of the quiescent initial conditions. This is continued into the interior on the $\alpha_-^{(0)}$ characteristic as

$$V_-(\alpha_-) = H(\alpha_- - \alpha_-^{(0)}), \qquad \text{(B-4)}$$
$$\alpha_-^{(0)} \equiv \gamma - \cos^{-1}s_0$$

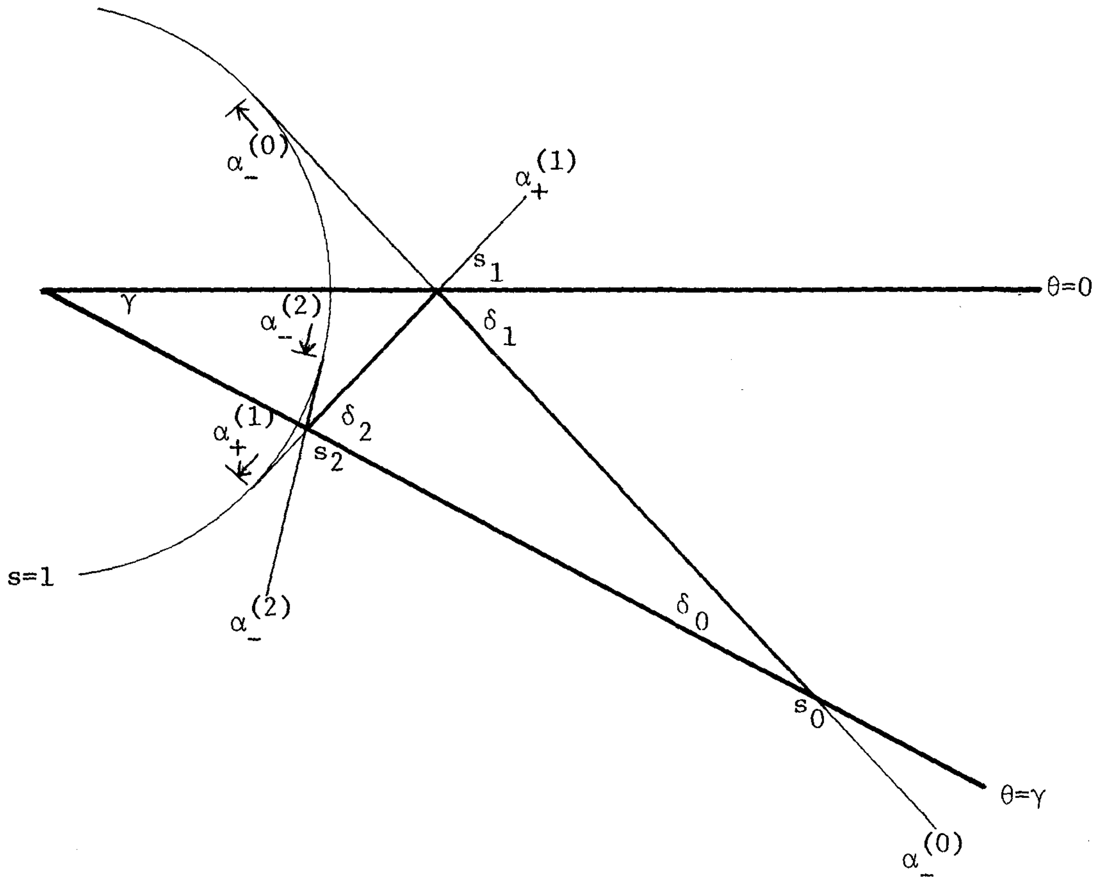
$\alpha_-^{(0)}$
$\alpha_+^{(1)}$
s_1
$\theta=0$
γ
$\alpha_-^{(2)}$
δ_1
$\alpha_+^{(1)}$
δ_2
s_2
$s=1$
$\alpha_-^{(2)}$
δ_0
s_0
$\theta=\gamma$
$\alpha_-^{(0)}$

Figure B-1. Wave system (characteristics) for a wedge angle, $\gamma=28^o$ and $V_o/c=3$.

where the wave makes an acute angle, δ_0,

$$\delta_0 \equiv \sin^{-1} s_0, \qquad \text{(B-5)}$$

with the lower face. This wave reflects off the free surface at s_1 with acute angle, δ_1,

$$s_1 = \sin(\gamma+\delta_0),$$

$$\delta_1 = \sin^{-1} s_1 = \gamma + \delta_0,$$

on the $\alpha_+^{(1)} = -\alpha_-^{(0)}$ characteristic with a reflection coefficient of unity from (A-11) (which could alternately be derived from (B-2)). The second reflection, off the lower face, occurs on the $\alpha_-^{(2)} = 2\gamma + \alpha_-^{(0)}$ characteristic at

$$s_2 = \sin(2\gamma+\delta_0),$$

with

$$\delta_2 = \sin^{-1} s_2 = 2\gamma + \delta_0,$$

and a sign change (a reflection coefficient of -1 from (A-11)) due to the high impedance mismatch. The wave terminates on the diffracted cylindrical front, $s = \frac{ct}{r} = 1$, at a critical angle denoted by $\theta_c (\theta_c = \alpha_-^{(2)}$ in Fig. B-1).

These results can be extended to arbitrary wedge angle by observing that the angle of incidence (or reflection) increases by γ, the wedge angle, at each reflection. Consequently the n^th internal reflection has an incidence angle of

$$\delta_n = n\gamma + \delta_0, \qquad \text{(B-6)}$$

and this occurs at

$$s_n = \sin\delta_n, \qquad \text{(B-7)}$$

where the reflection is off the free surface when n is odd and off the interface when n is even. Noting that $\delta_n < \pi/2$, from (B-6)

$$n < \frac{\pi/2-\delta_0}{\gamma},$$

hence the total number of internal reflections, I, is given by the number-theoretic function

$$I \equiv \mathrm{Int}\left(\frac{\pi/2-\delta_0}{\gamma}\right), \tag{B-8}$$

where Int ( ) gives the integral part of the argument. The number of reflections off the free surface, J, is

$$J = \begin{cases} I/2 & I \text{ even} \\ \mathrm{Int}(I/2) + 1 & I \text{ odd} \end{cases} . \tag{B-9}$$

The last reflection, at s_I, terminates on the diffracted front at θ_c where

$$\theta_c = \begin{cases} \gamma-\cos^{-1}s_I = (I+1)\gamma + \delta_0-\pi/2 & I \text{ even} \\ \cos^{-1}s_I = \frac{\pi}{2} - (I\gamma+\delta_0) & I \text{ odd} \end{cases} . \tag{B-10}$$

These formulas completely characterize the system of wavefronts.

Summing the jumps across the fronts yields the overall response, in particular at the surface. For example, consider Fig. B-2a,b. Across the wave between s_0 and s_1 (denoted by s_0s_1) there is a unit jump in particle velocity, v. This jump reflects in kind (a reflection coefficient of 1) off the free surface at s_1, hence across the s_1s_2 wave the velocity increases by unity again (yielding v = 2 behind s_0s_1 and s_1s_2). Upon reflection at s_2 the sense of the velocity jump reverses (a reflection coefficient of -1) and the velocity decreases by unit across the reflected wave. This wave can either terminate on s = 1 as in Fig. B-2a or reflect again off the free surface as in Fig. B-2b. Note that on the diffracted front, s = 1, particle velocity either increases or decreases by unity along the front as θ passes the point of termination, θ_c, depending on whether the number of free surface reflections, J (Eq. (B-9)), is even or odd, respectively.

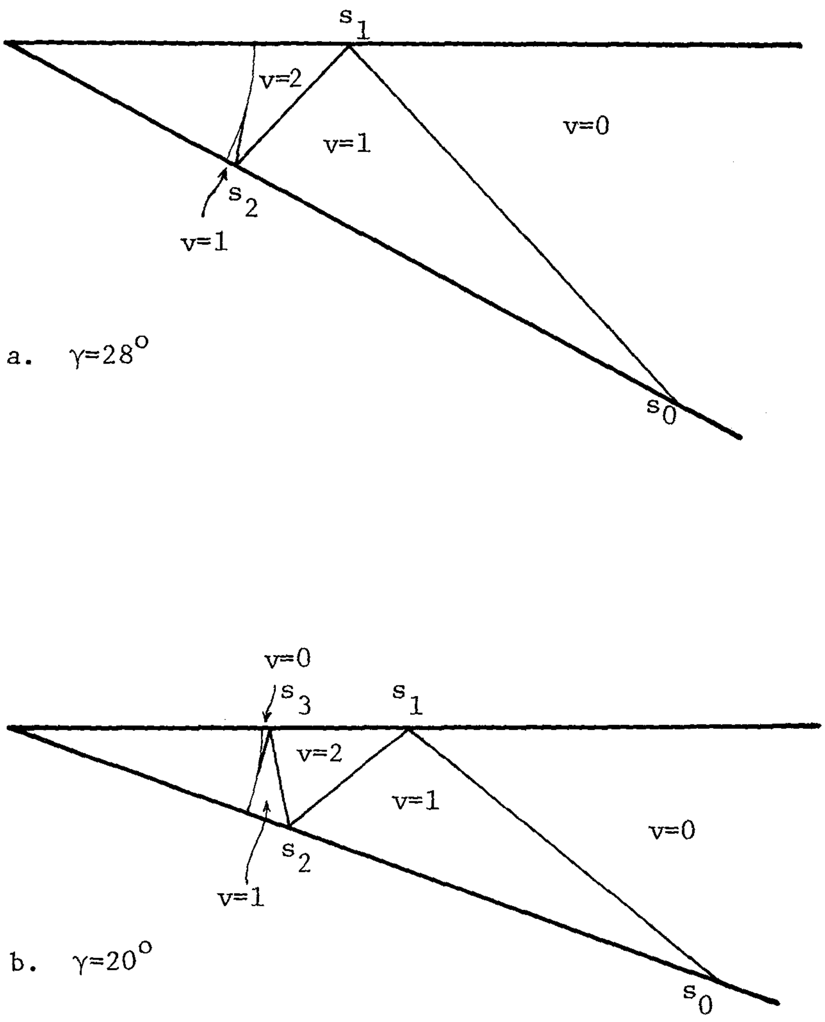
s1
v=2
v=1
v=0
s2
v=1
a. γ=28°
s0
v=0
s3
s1
v=2
v=1
v=0
s2
v=1
b. γ=20°
s0

Figure B-2. Plane waves and velocity response for $\gamma=28^{\circ}$ and $\gamma=20^{\circ}$ ($V_o/c=3$).

APPENDIX C

SELF-SIMILAR WEDGE SOLUTIONS IN THE ELLIPTIC DOMAIN

It has been shown in the self-similar formulation of the wedge problem that the solution for particle velocity in the elliptic domain (i.e., for $s \equiv \frac{ct}{r} > 1$) can be written as

$$v = \text{Re } V(\alpha), \qquad \text{(C-1)}$$

$$\alpha \equiv \theta + i \cosh^{-1} s,$$

where $V(\alpha)$ is an analytic function of the complex variable, α, over a semi-infinite strip in the α plane. In order to solve for $V(\alpha)$ it is convenient to map the semi-infinite strip onto a halfplane, where the solution is constructed by means of analytic function theory.

The succession of mappings from the physical domain, to the semi-infinite strip, to the halfplane are illustrated in Fig. C-1. The Schwarz-Christoffel transformation,

$$\frac{1}{\zeta} = \frac{1}{\xi+i\eta} = \cos\frac{\pi\alpha}{\gamma} \qquad \text{(C-2)}$$

$$= \cos\frac{\pi\theta}{\gamma}\cosh\left(\frac{\pi}{\gamma}\cosh^{-1}s\right) - i \sin\frac{\pi\theta}{\gamma}\sinh\left(\frac{\pi}{\gamma}\cosh^{-1}s\right),$$

was used to map the interior of the strip to the upper halfplane.

Boundary conditions in the physical domain determine those on the strip and halfplane. Conditions on the wedge faces for $s > 1$ are

$$\theta = 0: \quad v_\theta = 0 \, , \qquad \text{(C-3)}$$

$$\theta = \gamma: \quad v_s = 0 \, , \qquad \text{(C-4)}$$

while on the diffracted cylindrical front

$$s = 1: \quad v_\theta = (-1)^J \delta(\theta-\theta_c), \qquad \text{(C-5)}$$

where θ_c, the angle of termination, is given by (B-10). The sign is positive

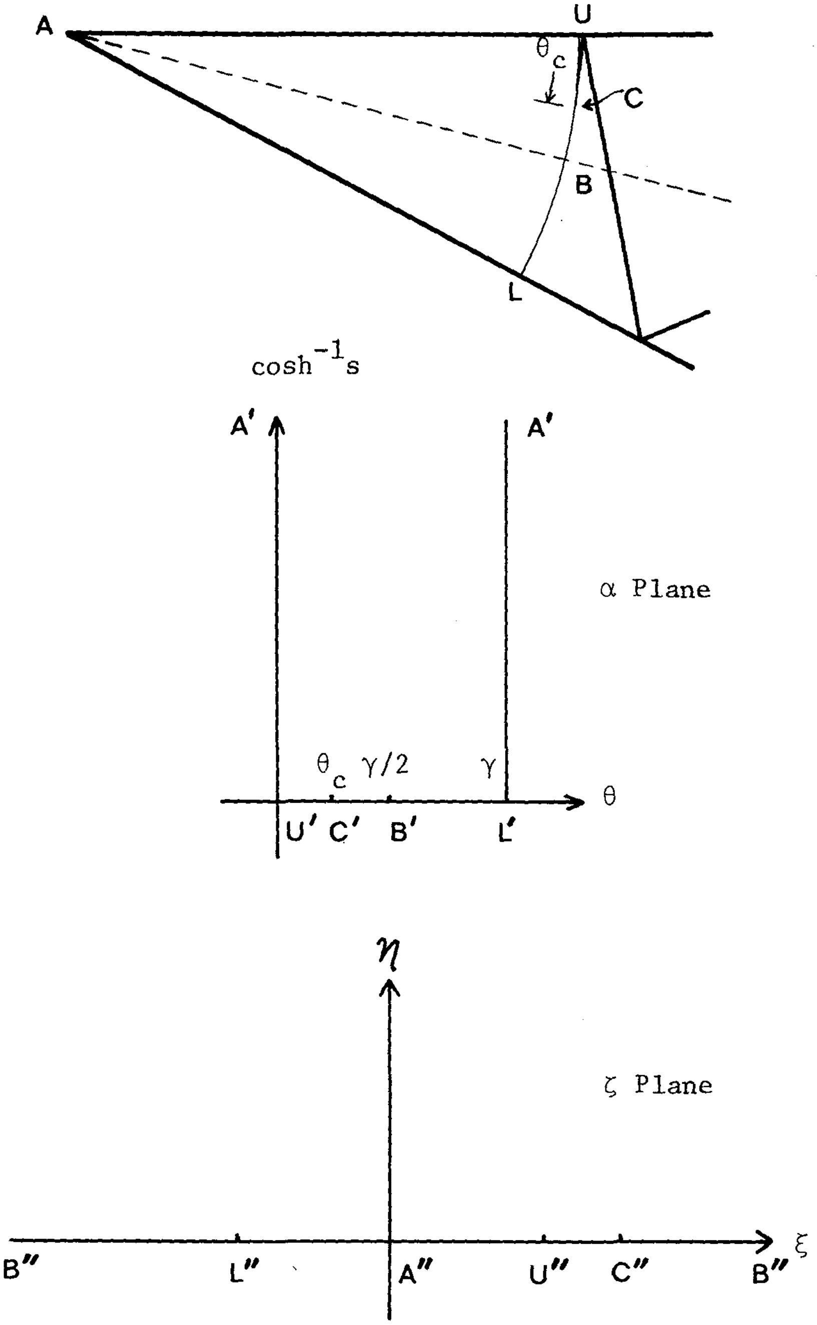
A
U
θc
C
B
L
cosh⁻¹s
A′
A′
α Plane
θc
γ/2
γ
θ
U′
C′
B′
L′
η
ζ Plane
B″
L″
A″
U″
C″
B″
ξ

Figure C-1. Succession of mappings from the physical domain to the α and ζ complex planes.

when the number of free surface reflections, J (see (B-9)) is even, and negative when J is odd, as discussed at the end of Appendix B. In order to apply these conditions to the analytic function, V, its derivative is expressed as

$$V'(\alpha) = v_\theta - i\sqrt{s^2-1}\ v_s\ , \qquad \text{(C-6)}$$

whence (C-3,4,5) are converted to conditons on the real and imaginary parts of V'. Therefore, on the boundaries of the strip in the complex α plane, conditions become

$$A'U':\quad v_\theta = 0 \Rightarrow \mathrm{Re}\ V' = 0, \qquad \text{(C-7)}$$

$$A'L':\quad v_s = 0 \Rightarrow \mathrm{Im}\ V' = 0, \qquad \text{(C-8)}$$

$$U'L':\quad v_\theta = (-1)^J\delta(\theta-\theta_c) \Rightarrow \mathrm{Re}\ V' = (-1)^J\delta(\theta-\theta_c). \qquad \text{(C-9)}$$

By virtue of the conformal transformation the above conditions apply directly to corresponding segments of the real axis in the complex ζ plane. The presence of the delta function at θ_c requires that V' has a simple pole at C". Also, at infinity, corresponding to the mapping of the bisector, B, it can be shown using (C-6) that Im V' goes to a constant. A form for $V'(\alpha)$ in the ζ plane which exhibits the pole, the proper order at infinity and the boundary behavior can be written directly as

$$V'(\alpha(\zeta)) = \kappa\,\frac{i\sqrt{\zeta(\zeta+1)}}{\zeta-\xi_c}\ , \qquad \text{(C-10)}$$

where $\xi_c = 1/\cos\frac{\pi\theta_c}{\gamma}$ is the location of C" and κ is a real constant related to the residue at ξ_c. κ is determined by evaluating $V'(\alpha(\zeta))$ on the real axis as

$$\lim_{\eta\to 0^+} V'(\alpha(\zeta)) = \kappa\ i\sqrt{\xi(\xi+1)}\left[\frac{1}{\xi-\xi_c} - i\pi\delta(\xi-\xi_c)\right]\ , \qquad \text{(C-11)}$$

and substituting the real part into (C-9), giving

$$\pi\kappa\sqrt{\xi_c(\xi_c+1)}\ \delta(\xi-\xi_c) = (-1)^J\delta(\theta-\theta_c).$$

Making use of the identity,

$$\delta(\xi-\xi_c) \equiv \frac{1}{\left|\frac{d\xi}{d\theta}\right|_{\theta=\theta_c}} \delta(\theta-\theta_c)$$

$$= \frac{\gamma}{\pi} \frac{\sin\frac{\pi\theta_c}{\gamma}}{\cos^2\frac{\pi\theta_c}{\gamma}} \delta(\theta-\theta_c) ,$$

and solving for κ gives

$$\kappa = (-1)^J \frac{1}{\gamma} \frac{\tan\frac{\pi\theta_c}{\gamma}}{\sqrt{1+\cos\frac{\pi\theta_c}{\gamma}}} . \tag{C-12}$$

Of interest here is the free surface response for which $\zeta = 1/\cosh(\frac{\pi}{\gamma}\cosh^{-1}s)$ From (C-6) and (C-10)

$$v_s = - \frac{1}{\sqrt{s^2-1}} \text{Im } V'(\alpha)$$

$$= - \frac{\kappa}{\sqrt{s^2-1}} \frac{\sqrt{\zeta(\zeta+1)}}{\zeta-\xi_c} . \tag{C-13}$$

Substituting (C-12) and rearranging yields on the free surface

$$v_s = \frac{(-1)^J}{\gamma} \frac{\sin\frac{\pi\theta_c}{\gamma}}{\sqrt{1+\cos\frac{\pi\theta_c}{\gamma}}} \cdot \frac{1}{\sqrt{s^2-1}} \frac{\sqrt{1+\cosh(\frac{\pi}{\gamma}\cosh^{-1}s)}}{\cosh(\frac{\pi}{\gamma}\cosh^{-1}s)-\cos\frac{\pi\theta_c}{\gamma}} . \tag{C-14}$$

This is the final result of the analytical procedure. Note that v_s vanishes identically when $\theta_c = 0$, from which v is a constant, equal to unity. As $\theta_c \to \gamma$

the solution is indeterminate, however L'Hospital's rule yields

$$\lim_{\theta_c \to \gamma} v_s = \frac{(-1)^J \sqrt{2}}{\gamma \sqrt{s^2-1} \sqrt{1+\cosh(\frac{\pi}{\gamma}\cosh^{-1} s)}} \tag{C-15}$$

In terms of particle acceleration the solution for v_s can be interpreted as follows. Since v is self-similar, $tv_t = sv_s$, but $v_t = \frac{1}{v_o} w_{tt}$ (recall $w_t = v_o v$) hence acceleration is $w_{tt} = \frac{v_o c}{r} v_s$.